Acta Geotechnica (2026) 21:2847–2871
https://doi.org/10.1007/s11440-025-02892-5

RESEARCH PAPER

Identification of the critical state line of sands using coupled shear-volumetric strain paths

Abhinanda Dilip[1] · Yide Wang[2] · Orestis Adamidis[1]

Received: 30 January 2025 / Accepted: 30 November 2025 / Published online: 21 January 2026
© The Author(s) 2026

Abstract

The identification of the critical state line projection in void ratio–mean effective stress ($e - p'$) space is an essential step in the characterization of a sand, needed both for estimations of shear strength and as input for advanced constitutive models. However, the determination of the critical state line is often an arduous process. In triaxial testing, it can be challenging to impose the large strains ($> 20\%$) required to attain the critical state without excessively distorting the sample. Moreover, the axial load required to reach the critical state under high initial confining stress can be beyond the capacity of typical soil testing equipment or instrumentation. Further, the pore pressure of dilative specimens subjected to undrained compression can drop enough to reach cavitation. This paper demonstrates how in such cases, the critical state line in $e - p'$ space can be indirectly derived through triaxial compression tests with coupled shear-volumetric strain paths that do not require axial strain beyond 15%. Congleton sand is used as an example. The process proposed is based on the observation that the locus of post-phase transformation and post-peak stress ratio instability points obtained from triaxial compression tests under the same strain coupling ratio represents a single curve in $e - p'$ space. The distance of this curve from the critical state is dependent on the strain coupling ratio and can be quantified within the context of double surface plasticity constitutive models through a modified state parameter function. Going further, this paper shows how the coupled strain experiments used to derive the critical state line can also serve for the calibration of additional double surface plasticity model parameters, with the final calibration shown to adequately capture triaxial compression tests under both undrained and coupled strain conditions.

Keywords Congleton sand · Critical state line · Model calibration · Partial drainage · SANISAND · Triaxial testing

Abbreviations

CSL	Critical State Line
LCSI	Locus of Constant State parameter Instabilities
PSRS	Peak Stress Ratio State
PTS	Phase Transformation State
α	Back-stress ratio
α^b, M^b	Slope of bounding surface
α^c, M_c	Slope of critical surface
α^d, M^d	Slope of dilatancy surface
$\dot{\epsilon_v}$	Volumetric strain rate
$\dot{\epsilon_q}$	Deviatoric strain rate
$\dot{\epsilon_1}$	Axial strain rate
$\dot{\epsilon_v^p}$	Plastic volumetric strain rate
$\dot{\epsilon_v^e}$	Elastic volumetric strain rate
$\dot{\epsilon_q^p}$	Plastic deviatoric strain rate
$\dot{\epsilon_q^e}$	Elastic deviatoric strain rate
ζ	$\dot{\epsilon_v}/\dot{\epsilon_1}$
η	Stress ratio ($= q/p'$)
Λ	$\dot{\epsilon_v}/\dot{\epsilon_q}$ ($= \frac{3\zeta}{3-\zeta}$)
ν	Poisson's ratio
σ	Standard deviation
ϕ	Friction angle
ψ	State parameter
ψ_F	State parameter form
ψ_D	State parameter definition

✉ Orestis Adamidis
orestis.adamidis@eng.ox.ac.uk

Abhinanda Dilip
abhinanda.dilip@eng.ox.ac.uk

Yide Wang
yide_wang@outlook.com

[1] Department of Engineering Science, University of Oxford, Parks Road, Oxford OX1 3PJ, UK

[2] Institute of Engineering Mechanics, China Earthquake Administration, 29, Xuefu Road, Nangang District, Harbin 150000, Heilongjiang Province, China

Ω	State parameter form constants
A_d, n^d, k^d	Positive dilatancy parameters
c	Ratio of slope of surfaces in triaxial extension to triaxial compression
C_u	$= d_{60}/d_{10}$ coefficient of uniformity
C_c	$= {d_{30}}^2/(d_{10}\text{x}d_{60})$ coefficient of curvature
d_x	Particle size for which (x)% of the material is finer
D	Dilatancy
D_r	Relative density
e	Void ratio
e_{in}	Initial void ratio
e_{INST}	Void ratio at instability
e_{max}	Maximum void ratio
e_{min}	Minimum void ratio
G, K	Elastic shear and bulk moduli, respectively
G_0	Elastic shear modulus model parameter
G_s	Specific gravity of solids
h, h_0, c_h	Hardening parameters
H	Hardening modulus
I_s	State index
m	Half angular opening of the yield surface $(= \lvert\eta - \alpha\rvert)$
n^b, k^b	Positive bounding parameters
q	Deviatoric stress
p'	Mean effective stress
p'_{in}	Initial mean effective stress
p'_{INST}	Mean effective stress at instability
P_{at}	Atmospheric pressure
R, Q	Critical state line material constants
V_s	Shear wave velocity
w	State parameter fitting constant
$\ddot{W}$	Second-order work
$\boldsymbol{\sigma}'$	Effective stress tensor
$\boldsymbol{\epsilon}$	Strain tensor

1 Introduction

The critical state line (CSL) is the fundamental ingredient of critical state soil mechanics [38]. Roscoe et al. [36] define the critical state as the state achieved at large strains, where unlimited shear deformation can occur with no change in volume, at constant normal and shear stress. Though the framework of critical state soil mechanics was initially developed for clays, the CSL is commonly employed in modelling of sand behaviour. Another term, the 'steady state' has also been in use for sands. It is defined by Poulos [34] as follows: 'The state in which the mass is continuously deforming at constant volume, constant normal effective stress, constant shear stress, and constant velocity. The steady state of deformation is achieved only after all particle orientation has reached a statistically steady state condition and after all particle breakage, if any, is complete so that the shear stress needed to continue deformation and the velocity of deformation remain constant'. The critical and steady state have in practice often been used without distinction [7]. Here, the term critical state will be used and the locus of points that reach this state will be referred to as the CSL, as this terminology is common within the context of double surface plasticity models, though the authors acknowledge that some of the fabric considerations of the anisotropic critical state theory (e.g., [27, 43]) are more aligned with the steady state definition.

The behaviour of a sand element can be predicted by its proximity to the CSL in $e - p'$ space. This observation was made by Roscoe [35], but it is the state parameter ψ, introduced by Been and Jefferies [6] as 'the void ratio difference between the initial sand state and the steady state conditions at the same mean effective stress', that has predominantly been used to evaluate behaviour. Indeed, ψ is a crucial parameter in many advanced constitutive models for sands (e.g., [9, 12, 19, 21, 24–26, 28, 29, 32, 41, 51]).

The CSL of a sand can be experimentally determined as a locus of points in $e - p'$ space, obtained by shearing specimens to large strains, until the critical state is reached. However, these points can be challenging to obtain for many sands. Triaxial compression to critical state often requires large axial strains ($> 20\%$) that can result in excessive deformations or localization of shearing. Such strains are beyond what most standards allow (e.g., ASTM D7181-20, ASTM D4767-11R20 and ASTM D2850-24) and can render the interpretation of 'element' behaviour challenging, not least because of area correction requirements. In addition, for critical state points at high mean effective stresses, the load limits of available testing equipment or instrumentation might be reached prior to the attainment of the critical state. Finally, very dilative sands can lead to negative pore water pressures during undrained compression and potential cavitation, which also prevents a specimen from reaching the critical state, unless a sufficiently high back pressure can be applied. For instance, Verdugo and Ishihara [46] had to design a high pressure triaxial cell with maximum pressure of 5 MPa to avoid cavitation in highly dilative specimens of Toyoura sand. Due to these impediments, researchers often have to rely on a fraction of conducted tests to define the CSL. Azeiteiro et al. [4] report 4 triaxial compression tests out of 14 as having reached the critical state for Hostun sand, while Dilip and Adamidis [13] report for the same sand that 4 out

of 15 triaxial compression tests reached the critical state. To overcome these physical limitations, in this study we propose an alternative method of determining the CSL, through a novel, analytically based experimental approach using coupled shear-volumetric strain paths. Note that within the context of this paper, a unique CSL assumption is made, which is expected to be valid for the levels of stress used in most geotechnical engineering applications, where the effects of particle breakage are negligible and particle rearrangement remains the predominant mechanism for shear deformation [5].

Coupled shear-volumetric strain paths have been previously experimentally investigated on loose and dense sands to quantify the significance of conditions other than undrained or fully drained, typically regarding strain-softening and instability triggering [10, 11, 14, 15, 20, 25, 30, 39, 40, 44, 45, 48]. Strain-softening under such paths has been experimentally shown to depend on the initial soil state and the strain increment ratio. Similarly to loose sands undergoing instability at peak deviator stress under undrained conditions, it has been demonstrated that dense sands can also become unstable above a threshold coupling strain rate, which is equal to the maximum $\dot{\epsilon_v}/\dot{\epsilon_1}$ obtained from drained compression tests. Note that the instability pursued in these studies arises purely from material behaviour rather than geometrical effects, such as necking in extension tests.

State-dependent constitutive models have been shown to adequately capture such coupled strain behaviour in direct simple shear and axisymmetric compression tests [21, 24, 25]. Hill's stability criterion [17] has been used to detect the onset of instability. For direct simple shear tests, the stress ratio at instability varies with the state parameter and the imposed strain coupling ratio [25]. Note that the instability points examined in these experimental and numerical investigations mostly pertain to contractive sand behaviour and are observed pre-phase transformation. The onset of instability using macro- and micro-scale second-order work criteria under coupled shear-volumetric strain paths has also been studied using discrete element method (DEM) investigations, where the instability behaviour has been observed to be closely related to the evolution of fabric anisotropy [37, 50]. Kamai and Boulanger [21] simulated the large strain behaviour of direct simple shear tests under coupled shear-volumetric strain using the PM4Sand constitutive model [9] and found that paths in $e - p'$ space become parallel to the CSL after considerable straining.

Drawing from the above observations, Dilip and Adamidis [13] demonstrated both using experiments and the SANISAND 2008 constitutive model [41] that the locus of post-phase transformation and post-peak stress ratio instability points obtained from coupled shear-volumetric strain triaxial compression tests, called here the Locus of Constant State parameter Instability (LCSI), represents a constant state parameter curve in $e - p'$ space, with the value of the state parameter linked to the strain coupling ratio. These instability points are related to the 'limit locus' of Imposimato and Nova [18] and are only observed for expansive strain coupling ratios. Note that the pre-phase transformation instability points typically examined in literature for flow liquefaction triggering do not fall on this constant state parameter curve. The LCSI curves for Hostun sand were found in [13] to be optimally represented using an updated state parameter definition ψ_D, which was incorporated in the selected SANISAND model and was shown to significantly improve simulations of coupled strain triaxial compression tests.

In this study, we use the LCSI framework to indirectly evaluate the CSL in $e - p'$ space for Congleton sand, a sand for which we were unable to directly obtain CSL points through undrained triaxial compression tests due to the physical limitations discussed before. First, LCSI curves were experimentally obtained in $e - p'$ space by conducting triaxial compression tests under three strain coupling ratios, ζ $(= \dot{\epsilon_v}/\dot{\epsilon_1})$, with specimens sheared to no more than 15% axial strain. The LCSI curve obtained experimentally for each strain coupling ratio was then used to back-calculate the CSL and the ψ_D function. This methodology was first validated by comparing the predicted CSL of Hostun sand with the known (experimentally determined) CSL of Hostun sand from Dilip and Adamidis [13]. Further use of the coupled strain experiments to calibrate the SANISAND 2008 model [41] was also explored. It was found that the conducted coupled strain compression tests under three strain coupling ratios can be used to obtain not only the CSL in $e - p'$ space and the ψ_D, but also the critical and the bounding surface stress ratios. The calibrated constitutive model was subsequently shown to adequately capture both undrained and coupled strain experiments. Thus, the contribution of this paper is threefold: first, it proposes a novel, analytically based experimental approach to estimate the CSL for sands where directly obtaining it is not possible; second, it demonstrates the extent to which the coupled strain triaxial compression tests required to derive the CSL can be further used to calibrate SANISAND models; and third, it provides calibration parameters for Congleton sand within the SANISAND framework.

2 Methodology

This section presents both the analytical and experimental methods used in this paper. Firstly, the constitutive equations of the SANISAND 2008 model [41] that are pertinent

to this study are listed, though conclusions would be similar for other SANISAND family models since our focus is on monotonic loading. Subsequently, a brief summary of the LCSI analytical framework demonstrated by Dilip and Adamidis [13] is given. Finally, an overview of the experimental methods used to perform coupled shear-volumetric strain triaxial compression tests is presented.

2.1 SANISAND formulation

SANISAND 2008 [41] is a critical-state compatible bounding surface plasticity model that aims to capture the monotonic and cyclic behaviour of sands across a range of densities and stresses. The yield surface within which stress states remain elastic is in the shape of a narrow closed wedge. Plastic strains are accumulated under changing stress ratio loading when stress states fall on the arms of the wedge, with the rotation of the bisector of the wedge representing kinematic hardening. The end cap is activated when constant stress ratio loading produces plastic strains, such as those related to particle crushing, and its translation captures isotropic hardening.

The surfaces controlling behaviour include the bounding surface, which controls the peak stress ratio, and the dilatancy surface, which controls the phase transformation stress ratio (Eqs. 1 and 2, respectively). The two surfaces are dependent on the state parameter, ψ, and the critical surface back-stress ratio, α^c, either in an exponential or linear form as shown in Eqs. (1) and (2). The linear form was used to develop the analytical framework for LCSI curves by Dilip and Adamidis [13]. Parameters n^b, k^b, n^d and k^d are positive constants. The slopes of the surfaces in triaxial extension are determined by multiplying parameter c to the slopes of the surfaces in triaxial compression. At the critical state, $\psi \rightarrow 0$ and all three surfaces converge to the critical state surface.

$$\alpha^b = \alpha^c exp(-n^b \psi) \; or \; \alpha^b = \alpha^c - k^b \psi \tag{1}$$

$$\alpha^d = \alpha^c exp(n^d \psi) \; or \; \alpha^d = \alpha^c + k^d \psi \tag{2}$$

The hardening modulus, H, is a function of the distance between the bounding surface, α^b and the current stress ratio, α as noted in Eq. 3, with h a positive function of model constants and the current soil state. Dilatancy D is the ratio of the plastic volumetric strain increment ($\dot{\epsilon_v}^p$) to the plastic deviatoric strain increment ($\dot{\epsilon_q}^p$). For compression loading, it is a function of the distance between the dilatancy surface, α^d and the current stress ratio, α as shown in Eq. (4), with A_d as a positive dilatancy parameter.

$$H = h(\alpha^b - \alpha) \tag{3}$$

$$D = \frac{\dot{\epsilon_v}^p}{\dot{\epsilon_q}^p} = A_d(\alpha^d - \alpha) \tag{4}$$

The critical, bounding, and dilatancy surfaces described above are enough to generate the response of an element in triaxial compression. Other aspects of the SANISAND 2008 model, for instance those related to cyclic loading, do not get activated for the tests simulated here and are thus not further described, with the reader referred to Taiebat and Dafalias [41] for a full report.

2.2 Constant State Parameter Instability

Instability is identified by the loss of uniqueness of incremental response under any loading programme, which has been shown to be coincident with the second-order work being no longer positive definite [18]. The second-order work ($\ddot{W}$) refers to a sufficient condition of stability of the mechanical response of elastoplastic continua, also known as Hill's stability criterion [17], and is expressed at the element level for rate-independent media as shown in Eq. (5) [1, 24]. A positive second-order work implies a stable response, whereas a negative value indicates potential instability in the material. Thus, the positive definiteness of the second-order work ensures a unique material response. Equation (5) holds for proportional strain loading paths or coupled shear-volumetric strain paths examined in this study, of which the undrained loading is a special case [25, 31]. In triaxial space, Hill's criterion can be expressed using incremental stresses and strains, as shown in Eq. (6), following Andrade et al. [2].

$$\ddot{W} = \dot{\boldsymbol{\sigma}}' : \dot{\boldsymbol{\epsilon}} > 0 \tag{5}$$

$$\ddot{W} = \dot{p}'\dot{\epsilon_v} + \dot{q}\dot{\epsilon_q} > 0 \tag{6}$$

Dilip and Adamidis [13] numerically showed that when post-phase transformation and post-peak stress ratio instability points are triggered under a constant ratio of volumetric to shear strain rate, the hardening modulus diminishes approximately to 0, forcing α to fall on α^b. Under this condition, dilatancy D was analytically shown to be equal to the imposed ratio of volumetric to deviatoric strain increment, $\Lambda(= \dot{\epsilon_v}/\dot{\epsilon_q})$ which can be also expressed as a function of the imposed strain coupling ratio, $\zeta(= \dot{\epsilon_v}/\dot{\epsilon_1})$, as shown in Eq. (7). Note that the volumetric and deviatoric elastic strain increments aren't diminished at the instability points, but the ratio of the volumetric and deviatoric plastic strain increments (= D per Eq. 4) equals the ratio of total volumetric and deviatoric strain increments. The locus of such instability points produced by shearing isotropically consolidated samples at varying initial states (void ratio and mean effective stress) under the same strain coupling ratio constitutes the LCSI. Figure 1

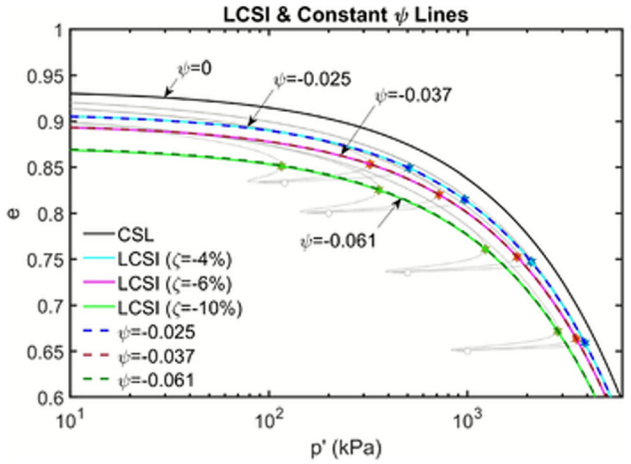

Fig. 1 Locus of Constant State parameter Instability points (LCSI) or Constant ψ Lines for coupled strain paths in triaxial space on Toyoura sand (reproduced from Dilip and Adamidis [13])

shows simulated LCSI curves for samples of Toyoura sand at varying initial states sheared under three strain coupling ratios [13]. The relevant instability points that constitute the LCSI are shown in solid star markers. The conditions at the LCSI are summarized in Eq. (7).

$$\text{At } LCSI, \alpha^b \approx \alpha \text{ and } D \approx \Lambda \text{ where } \Lambda = \frac{3\zeta}{3-\zeta} \tag{7}$$

Thus, using the linear dependency of SANISAND controlling surfaces on the state parameter (shown in Eqs. 1 and 2) and incorporating the conditions of Eq. (7) in Eq. (4), the LCSI curve can be described by Eq. (8) [13]. Since A_d, k^d and k^b are calibration constants, Eq. (8) implies that the state parameter ψ of LCSI points is a function of the imposed strain coupling ratio, ζ. Thus, all instability points obtained post-phase transformation and post-peak stress ratio under a given strain coupling ratio ζ correspond to the same state parameter ψ and therefore lie at a constant distance from the CSL in $e - p'$ space, as demonstrated in Fig. 1. As already stated, these are not the typical pre-phase transformation instability points examined for flow liquefaction triggering, for which the hardening modulus (Eq. 3) does not diminish to 0, i.e. $\alpha^b \neq \alpha$, as required to satisfy the LCSI (Eq. 7). Moreover, these instability points are only observed for expansive strain coupling ratios.

$$A_d(k^d\psi + k^b\psi) \approx \Lambda = \frac{3\zeta}{3-\zeta} \tag{8}$$

2.3 Experimental testing

Triaxial compression tests, conducted using a GDS advanced dynamic triaxial testing device are discussed in this paper. The capacity of the triaxial cell was 1 MPa. The testing protocol was based on ASTM D4767-11R20 and ASTM D7181-20 standards. All tests were performed on Congleton HST-95 sand, a poorly graded fine sand with predominantly rounded particles and a composition of at least 95% quartz [16]. The particle size distribution curve and a microscopy image are shown in Fig. 2. The sand properties obtained from physical characterization tests per DGI (Danish Geotechnical Institute) test method TM-406 for maximum and minimum dry density, are listed in Table 1. The specimens, prepared using the water (wet) pluviation technique, measured 70 mm in diameter and 140 mm in height. B-values of at least 98% were achieved for all tests. A compressive axial strain rate of 6 mm/hr was used. The back volume controller was used to impose a volumetric strain rate as a percentage of the axial strain rate for the coupled shear-volumetric strain tests. More information on the testing device, testing procedure and applied corrections can be found in Dilip and Adamidis [13].

3 Determination of the Critical State Line

In this section, a series of coupled shear-volumetric strain, triaxial compression experiments conducted on Congleton sand are presented, where instability points triggered post-phase transformation and post-peak stress ratio are highlighted. Based on the concept of LCSI explained earlier, each coupling ratio ζ corresponds to a different LCSI curve (Fig. 1). Further, each LCSI curve is related to the CSL through a constant state parameter value, following Eq. 8. In order to determine the CSL using the experimentally obtained LCSI curves, a method consisting of the following steps is proposed:

1. An appropriate state parameter form must be identified, which adequately fits the data and complies with the requirements of Eq. (8).
2. The available LCSI curves must be described as a function of the chosen state parameter form and an anticipated expression for the CSL (e.g., following Bolton [8]).
3. The CSL can finally be determined by setting the state parameter form equal to zero within the produced LCSI function.

This process is described in detail below, using experimental results for Congleton sand as an example. The process of locating the CSL is also validated using Hostun sand by comparing the predicted CSL with the known CSL from Dilip and Adamidis [13].

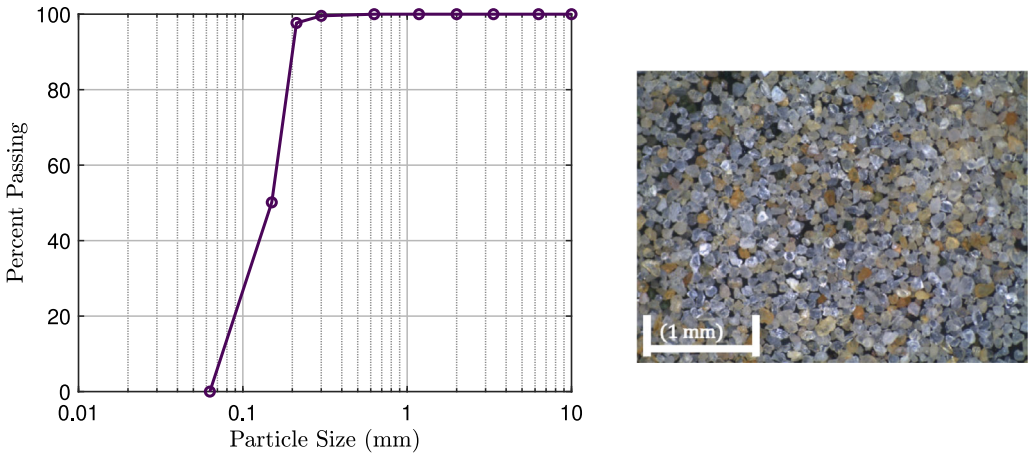

Fig. 2 Particle size distribution curve and microscopy image for Congleton sand, following Fleminger [16]

Table 1 Properties of Congleton sand

e_{max}	e_{min}	G_s	d_{50}	d_{10}	C_u	C_c
0.782	0.538	2.63	150μm	75μm	2.15	0.91

3.1 Experimental results

Conventional undrained and drained triaxial compression tests that were performed to locate the CSL of Congleton sand are listed in Table 2. None of the undrained or drained tests attained the critical state, as seen from the excess pore pressure and volumetric strain plots shown in Fig. 3. The undrained tests approached cavitation and the drained tests underwent excessive straining without having reached the critical state. Table 3 lists the triaxial compression tests performed under coupled volumetric and shear strains as part of this study to determine the CSL. Constant ratios of volumetric strain rate to axial strain rate, $\zeta = \dot{\epsilon_v}/\dot{\epsilon_1}$ were imposed and the LCSI points were determined using Eq. (6) and selecting points post-phase transformation and post-peak stress ratio. In the laboratory, the tests were strain-controlled and as such remained controllable beyond the instability points pursued here. Peak stress ratios are also listed in Table 3. All coupled strain experimental results are shown in $e - p'$ space in Fig. 4. Note that the pore pressures approached cavitation prior to triggering of instability for tests $P1$ and $P2$ under $\zeta = -10\%$, and the testing equipment reached its load limit prior to triggering

Table 2 Results of undrained and drained monotonic triaxial compression tests on Congleton Sand

Test ID[a]	$e_{in}{}^{b}$	$p'_{in}{}^{b}$	$e_{end}{}^{c}$	$p'_{end}{}^{c}$	$\eta_{end}{}^{c}$
ICUMC/0.586/100 (U1)	0.586	100.3	0.586	765.1	1.16
ICUMC/0.596/100 (U2)	0.596	200.3	0.596	1601.7	1.41
ICUMC/0.636/300 (U3)	0.636	299.8	0.636	1224.5	1.34
ICUMC/0.642/300 (U4)	0.642	299.9	0.642	1665.0	1.31
ICUMC/0.645/100 (U5)	0.645	100.4	0.645	872.2	1.37
ICUMC/0.658/100 (U6)	0.658	99.9	0.658	849.2	1.34
ICUMC/0.674/100 (U7)	0.674	100.0	0.674	1180.5	1.05
ICUMC/0.690/50 (U8)	0.690	50.2	0.690	1165.1	1.19
ICDMC/0.640/50 (D1)	0.640	49.3	0.721	80.9	1.01
ICDMC/0.628/100 (D2)	0.628	98.8	0.712	157.0	1.03
ICDMC/0.642/90 (D3)	0.642	88.4	0.728	160.0	1.07
ICDMC/0.646/300 (D4)	0.646	299.3	0.714	468.2	1.06
ICDMC/0.570/100 (D5)	0.570	99.5	0.690	162.0	1.08

[a](1) type of consolidation: IC for isotropic consolidation; (2) type of drainage: U for undrained, D for drained; (3) type of loading: MC for monotonic compression; (4) void ratio after consolidation; and (5) mean effective stress after consolidation. [b] Post consolidation values; [c] End of test

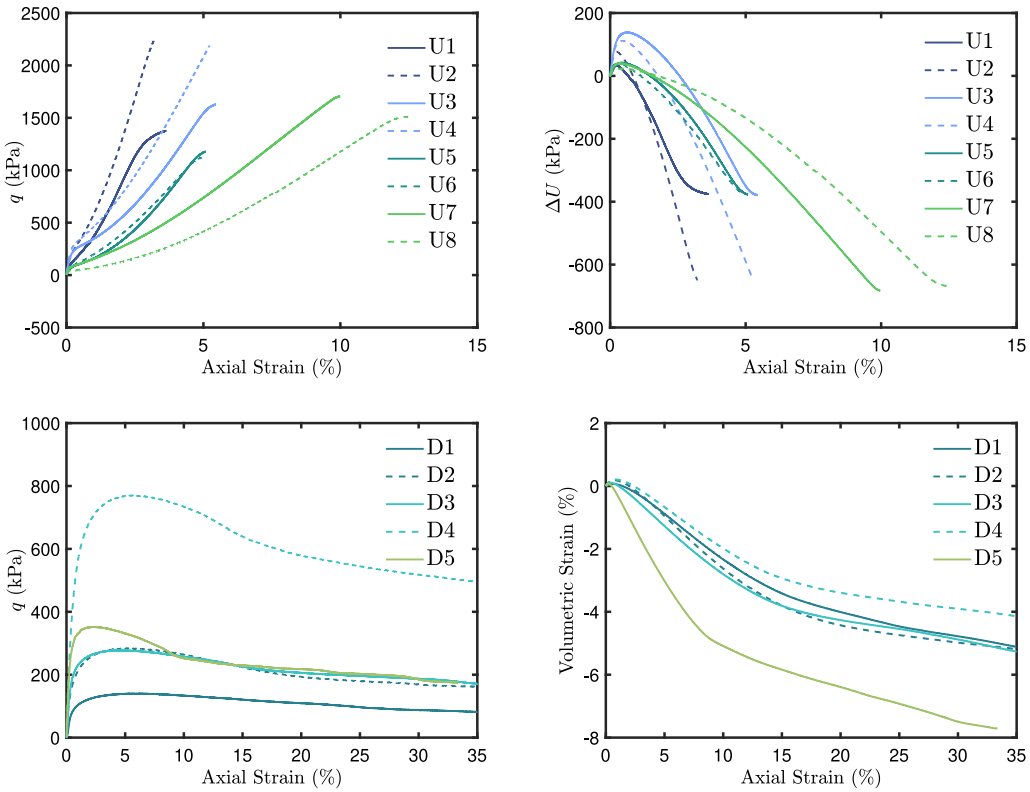

Fig. 3 Undrained (U) and drained (D) triaxial compression tests for Congleton sand from Table 2

of instability for tests $P4$ and $P6$ under $\zeta = -20\%$. For test $P5$, the instability point obtained using Hill's criterion did not satisfy the LCSI curve conditions given in Eq. (7) (post-phase transformation and post-peak stress ratio) and was therefore discarded.

3.2 State parameter form

The state parameter form, $f(p', e)$, must satisfy the LCSI curve instability points in $e - p'$ space. Additionally, it should also satisfy Eq. (8) through an adequate state parameter definition, that is a function of the state parameter form, $g(f(p', e))$. The state parameter form and the state parameter definition need not be the same. In the sequel, the state parameter form is denoted by ψ_F, whereas the state parameter definition is denoted by ψ_D, related to the ψ_F using Eq. (9). This distinction allows ψ_F to be selected without confirming that Eq. (8) is numerically satisfied for all experimental data. For instance, using Eq. (9) as the state parameter definition ψ_D, Dilip and Adamidis [13] showed that compliance with Eq. (8) was ensured for Hostun sand using a state parameter form $\psi_F = ln(e/e_{cs})$ and $w = 1.6$. A power law similar to Eq. (9) was first introduced in Li et al. [28] to represent a direct exponential dependence of the dilatancy parameter on the Been and Jefferies [6] state parameter. It is possible to determine the CSL through an appropriately selected ψ_F, without fully defining ψ_D, i.e. without knowing parameter w in Eq. (9). This is because at the CSL, $\psi_D = 0$ and $\zeta = 0$ or $\Lambda = 0$ (Eq. 8). Nevertheless, ψ_D needs to be defined in a way that satisfies Eq. (8) for $\zeta \neq 0$, if the constitutive model is to be used.

$$\psi_D = sign(\psi_F)|\psi_F|^w \Rightarrow \psi_F = sign(\psi_D)|\psi_D|^{1/w} \tag{9}$$

Two important conclusions regarding the nature of ψ_D and ψ_F can be drawn from Eq. (8) as listed below:

1. At each LCSI curve, ψ_D must hold a constant value, which implies that ψ_F must hold a constant value (e.g., Eq. (9)). Hence, an appropriate ψ_F can be selected to adequately describe the shape of all experimentally captured LCSI curves. For instance, if each LCSI curve is a vertical translation of another in $e - p'$ space, then the $\psi_F = e - e_{cs}$ of Been and Jefferies [6] can be deemed appropriate.
2. The state parameter definition ψ_D must be linearly related to Λ and thus take a zero value for points on the CSL, which in $e - p'$ space coincides with the LCSI under undrained conditions ($\zeta = 0 \Longleftrightarrow \Lambda = 0$). Note that as long as this criterion is satisfied, the CSL can be determined based on ψ_F, without fully defining ψ_D.

Table 3 Results of coupled strain monotonic triaxial tests on Congleton sand, performed under different values of $\zeta(=\dot{\epsilon_v}/\dot{\epsilon_1})$

Test ID[a]	e_{in}[b]	p'_{in}[b]	e_{INST}[c]	p'_{INST}[c]	η_{PSRS}[d]	ϕ_{PSRS}[d]	η_{end}[e]	ϕ_{end}[e]
ICPDMC/0.655/150/-10 (P1)	0.655	150	–	–	1.35	33.3°	1.32	32.7°
ICPDMC/0.633/150/-10 (P2)	0.633	150	–	–	1.36	33.8°	1.34	33.2°
ICPDMC/0.641/150/-20 (P3)	0.641	150	0.677	616.4	1.38	34.1°	1.19	29.9°
ICPDMC/0.587/150/-20 (P4)	0.587	150	–	–	1.45	35.8°	1.39	34.4°
ICPDMC/0.701/100/-20 (P5)	0.701	100	–	–	1.28	31.7°	0.79	20.5°
ICPDMC/0.615/300/-20 (P6)	0.615	300	–	–	1.40	34.7°	1.32	32.7°
ICPDMC/0.640/150/-30 (P7)	0.640	150	0.669	74.8	1.41	34.8°	1.13	28.4°
ICPDMC/0.657/100/-20 (P8)	0.657	100	0.688	127.4	1.36	33.7°	0.69	18.0°
ICPDMC/0.626/300/-30 (P9)	0.626	300	0.655	142.9	1.41	34.9°	1.14	28.7°
ICPDMC/0.662/30/-20 (P11)	0.662	30	0.698	154.5	1.39	34.3°	1.25	31.1°
ICPDMC/0.670/20/-20 (P12)	0.670	20	0.696	55.7	1.38	34.1°	0.88	22.6°
ICPDMC/0.595/500/-30 (P13)	0.595	500	0.635	1319.1	1.45	35.7°	0.67	17.6°
ICPDMC/0.590/300/-30 (P14)	0.590	300	0.633	1197.3	1.48	36.4°	1.12	28.2°
ICPDMC/0.680/10/-20 (P15)	0.680	10	0.705	35.7	1.54	37.7°	0.46	12.4°
ICPDMC/0.602/100/-40 (P16)	0.602	100	0.635	79.3	1.50	36.9°	1.35	33.3°
ICPDMC/0.582/300/-40 (P17)	0.582	300	0.624	702.1	1.50	36.9°	0.21	5.9°
ICPDMC/0.622/500/-30 (P19)	0.622	500	0.655	367.8	1.43	35.2°	0.78	20.3°
ICPDMC/0.581/200/-40 (P20)	0.581	200	0.621	490.5	1.52	37.4°	1.22	30.4°
ICPDMC/0.632/300/-20 (P21)	0.632	300	0.668	713.8	1.39	34.3°	1.19	29.7°
ICPDMC/0.610/30/-40 (P22)	0.610	30	0.639	34.2	1.60	39.2°	1.50	36.9°
ICPDMC/0.598/150/-40 (P24)	0.598	150	0.631	299.0	1.51	37.1°	1.31	32.4°
ICPDMC/0.636/100/-30 (P26)	0.636	100	0.663	55.7	1.44	35.6°	1.28	31.8°
ICPDMC/0.637/300/-30 (P27)	0.637	300	0.659	230.2	1.40	34.6°	0.76	19.6°
ICPDMC/0.611/200/-40 (P28)	0.611	200	0.643	168.7	1.48	36.4°	0.86	22.0°

[a](1) type of consolidation: IC for isotropic consolidation; (2) type of drainage: PD for partially drained; (3)type of loading: MC for monotonic compression; (4) void ratio after consolidation; (5) mean effective stress after consolidation; and (6) coupled strain ratio during the shearing stage, $\zeta = \dot{\epsilon_v}/\dot{\epsilon_1}$, in percentage. [b]Post consolidation values; [c]INST: Instability Point; [d]PSRS: Peak Stress Ratio State; [e]End of test

Considering the above conditions, an investigation on a state parameter form ψ_F for the Congleton sand results of Fig. 4 was undertaken. First, possible state parameter forms were assessed for their ability to consistently describe the shape of the LCSI curves. Different state parameter forms could be appropriate (e.g., [6, 8, 12, 23, 47, 49]). Here, the vertical distance in $e - p'$ space, $\psi_{F1} = e - e_{cs}$ [6] and the ratio of current void ratio to critical state void ratio $\psi_{F2} = e/e_{cs}$ [47] were examined.

Taking any two LCSI curves under strain coupling ratios ζ_i and ζ_j respectively, for each of the two ψ_F considered (ψ_{F1} and ψ_{F2}), a constant (Ω) can be derived that links the two LCSI curves. These constants are given in Eqs. (10) and (11), where void ratios e_ζ and e_{cs} correspond to the same (random) value of mean effective stress p'. Form 1 implies a constant vertical distance between the two LCSI curves in $e - p'$ space, while form 2 implies a constant ratio between the two LCSI curves.

$$\begin{aligned} &Form\ 1 : \psi_{F1,\zeta} = e_\zeta - e_{cs} \\ &\Rightarrow e_{\zeta_i} - e_{\zeta_j} = \psi_{F1,\zeta_i} - \psi_{F1,\zeta_j} = \Omega_1 \end{aligned} \tag{10}$$

$$\begin{aligned} &Form\ 2 : \psi_{F2,\zeta} = \frac{e_\zeta}{e_{cs}} \\ &\Rightarrow \frac{e_{\zeta_i}}{e_{\zeta_j}} = \frac{\psi_{F2,\zeta_i}}{\psi_{F2,\zeta_j}} = \Omega_2 \end{aligned} \tag{11}$$

To avoid the assumption of analytical expressions for the experimental LCSI curves, the assessment for the Ω constants discussed above was based directly on the available data points. This was achieved by selecting one of the LCSI sets of points as a reference and translating the other two LCSI sets of points to the reference through an appropriate Ω constant. As shown in Fig. 5, the LCSI point set corresponding to $\zeta = -20\%$ was selected as reference. For form 1 (Eq. 10 and Fig. 5a), an $\Omega_{1,i|j}$ was used to vertically translate each LCSI set corresponding to coupling ratio $'j'$ ($\zeta = -30\%$ and -40%) in $e - p'$ space to the reference set $'i'$ ($\zeta = -20\%$). For form 2 (Eq. (11) and

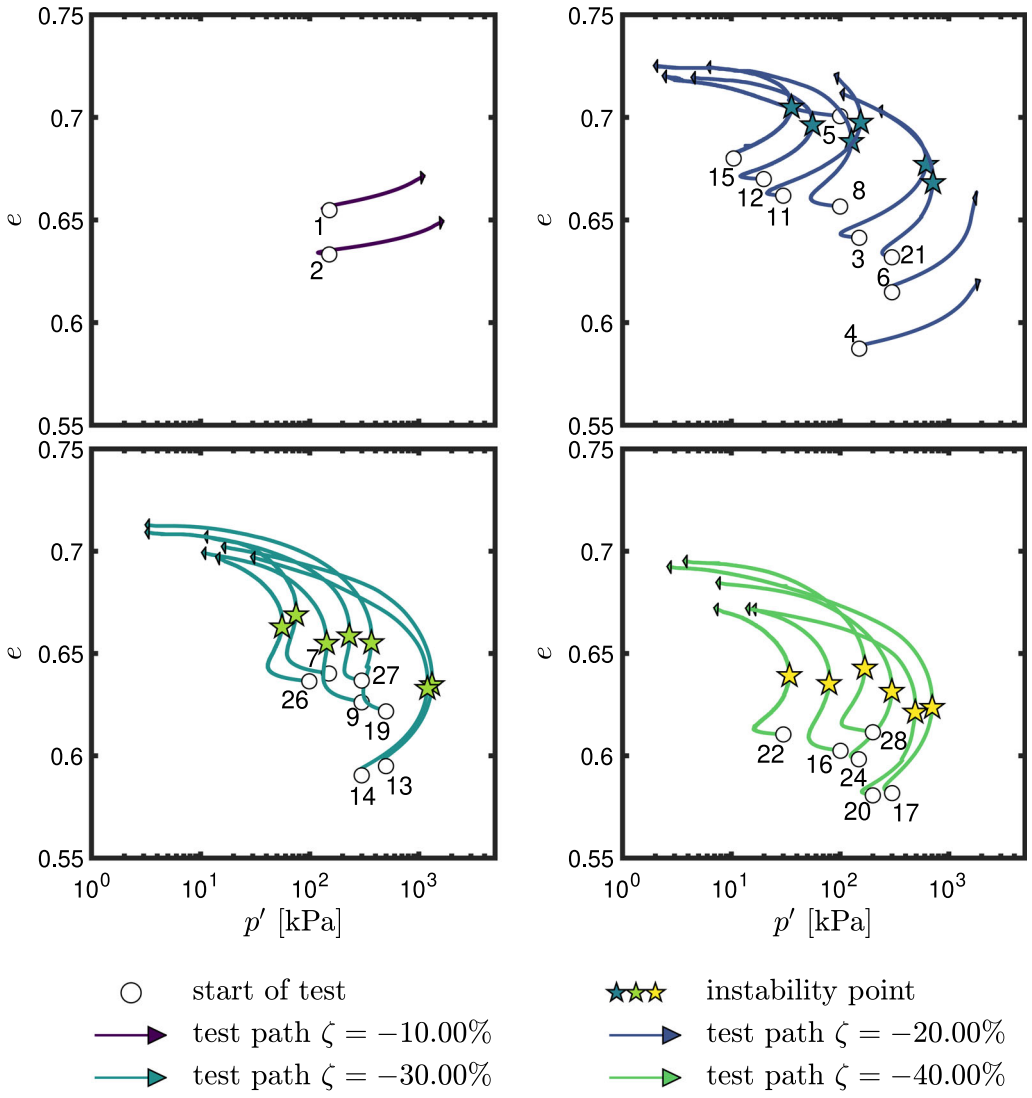

Fig. 4 Coupled strain tests with LCSI points under strain coupling ratio $\zeta(=\dot{\epsilon_v}/\dot{\epsilon_1})$ for Congleton sand

Fig. 5b) an $\Omega_{2,i|j}$ was used as a void ratio multiplication constant to move each 'j' ($\zeta = -30\%$ and -40%) LCSI set to the reference 'i' ($\zeta = -20\%$) in $e - p'$ space. The numerical values of the chosen Ω constants were selected to minimize the scatter of all data in $e - p'$ space, including the reference LCSI set ($\zeta = -20\%$) and the two translated sets ($\zeta = -30\%$ and $\zeta = -40\%$). The overall scatter was quantified through the mean of the moving standard deviation of e across the examined range of p'.

Figure 6 illustrates the selection process of Ω constants for both ψ_F considered (Eqs. 10 and 11). A range of values was scanned for each Ω constant. The moving standard deviation in void ratio was calculated as the standard deviation about the moving average across five adjacent points. The mean of the moving standard deviation is the value plotted on the vertical axis of Fig. 6, with its minimum value corresponding to the selected Ω constants as given in Table 4. Figure 5 shows all the obtained LCSI data points translated to the reference $\zeta = -20\%$ set using the constants of Table 4. Both state parameter forms explored (Eqs. 10 and 11) could be considered appropriate for the examined data, as both resulted in a mean of the moving standard deviation of e (~ 0.006), which was similar to the inherent scatter in the dataset of just the reference $\zeta = -20\%$ set.

A difference between the two definitions could become more prominent at higher mean effective stresses, when the slope of the CSL in $e - p'$ space becomes steeper, producing LCSI curves of different shape depending on the state parameter form assumed. Such a distinction could be made for the Hostun sand results of Dilip and Adamidis [13], where ψ_{F2} was deemed more appropriate. However, the steeper part of the CSL for Congleton sand is not expected to fall within the range of mean effective stresses

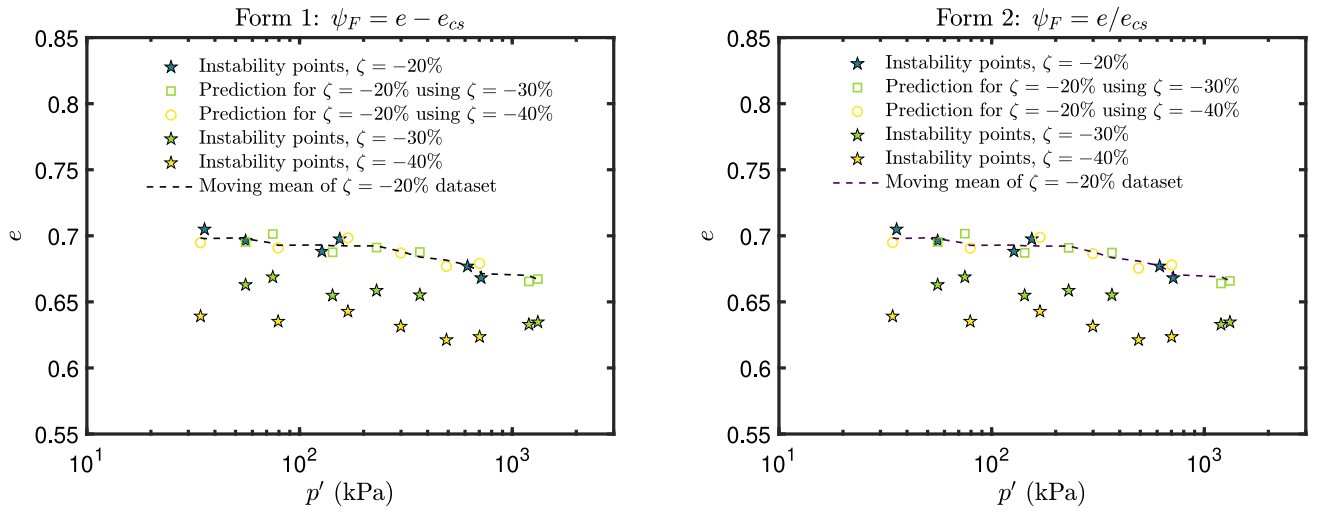

Fig. 5 Assessment of state parameter forms, **a** Form 1: $\psi_{F1,\zeta} = e_\zeta - e_{cs}$ and **b** Form 2: $\psi_{F2,\zeta} = \frac{e_\zeta}{e_{cs}}$, through transferring LCSI points for $\zeta = -30\%$ and -40% to the $\zeta = -20\%$ LCSI curve

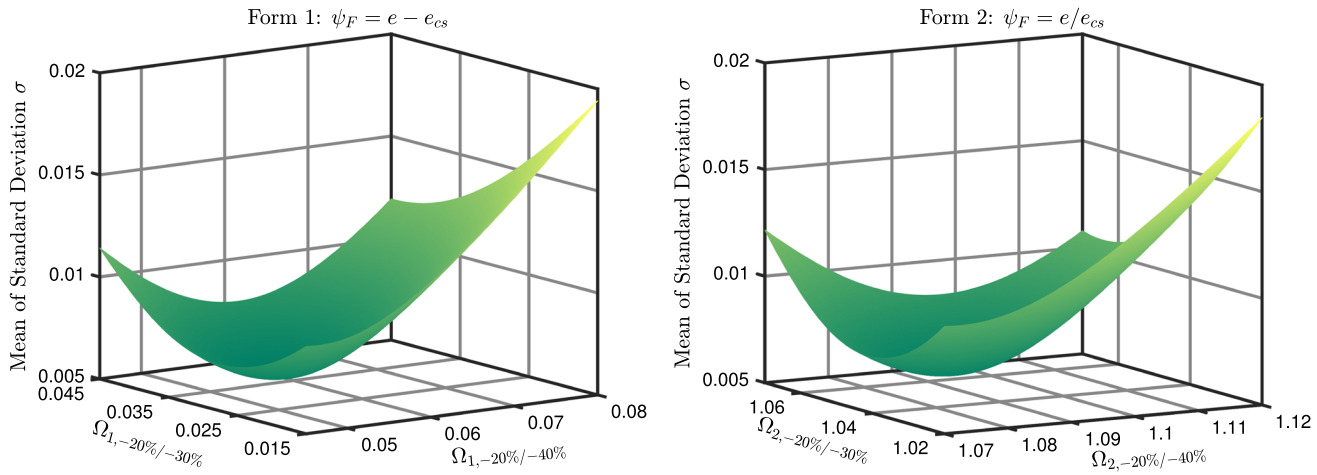

Fig. 6 Mean of moving (5 point) standard deviation of all experimentally obtained points translated to the reference $\zeta = -20\%$ LCSI curve based on state parameter forms (a) Form 1: $\psi_{F1,\zeta} = e_\zeta - e_{cs}$ and (b) Form 2: $\psi_{F2,\zeta} = \frac{e_\zeta}{e_{cs}}$

examined here (up to 1 MPa). As a result, both $\psi_{F1} = e - e_{cs}$ and $\psi_{F2} = e/e_{cs}$ can be considered as having adequately satisfied the criterion of describing the shape of the obtained LCSI experimental data.

The next step is to ensure that a state parameter definition ψ_D based on a selected form ψ_F can be found, that becomes zero for points on the CSL. If Eq. (9) applies, only the first form considered ($\psi_{F1} = e - e_{cs}$) produces a ψ_D

Table 4 Values for constants Ω_1 (based on state parameter form of Eq. (10)) and Ω_2 (based on state parameter form of Eq. (11)) resulting in the minimum mean of moving standard deviation

Reference set	Constant	Definition	Value
$\zeta = -20\%$	$\Omega_{1,-20\%\|-30\%}$	$e_{-20\%} - e_{-30\%}$	0.0326
$\zeta = -20\%$	$\Omega_{1,-20\%\|-40\%}$	$e_{-20\%} - e_{-40\%}$	0.0556
		Mean of moving σ	0.0058
$\zeta = -20\%$	$\Omega_{2,-20\%\|-30\%}$	$e_{-20\%}/e_{-30\%}$	1.0493
$\zeta = -20\%$	$\Omega_{2,-20\%\|-40\%}$	$e_{-20\%}/e_{-40\%}$	1.0877
		Mean of moving σ	0.0060

that satisfies this criterion. The second form ($\psi_{F2} = e/e_{cs}$) produces a ψ_D that becomes unity at critical state and is inadequate for the surface definitions of the constitutive model, Eqs. 1 and 2. However, it is possible to recast it in a way that preserves the observation of the above investigation, that a constant ratio between LCSI curves can adequately maintain their shape. The form ψ_{F3} shown in Eq. (12) produces a definition ψ_D based on Eq. (9) that satisfies the criterion of being zero at critical state, while it is positive for $e > e_{cs}$ and negative for $e < e_{cs}$.

$$\psi_{F3} = ln\left(\frac{e}{e_{cs}}\right) \tag{12}$$

Additionally, it maintains a constant ratio between two LCSI curves, at ζ_i and ζ_j, as demonstrated in Eq. (13) ($\Omega_3 = \Omega_2$) and is thus satisfactory in terms of describing the shape of the captured LCSI data points based on the previous investigation.

$$\begin{aligned} &Form\ 3: \psi_{F3,\zeta} = ln\left(\frac{e_\zeta}{e_{cs}}\right) \\ &\Rightarrow \frac{e_{\zeta_i}}{e_{\zeta_j}} = exp\left(\psi_{F3,\zeta_i} - \psi_{F3,\zeta_j}\right) = \Omega_3 = \Omega_2 \end{aligned} \tag{13}$$

Alternatively, the state parameter form $\psi_{F2} = e/e_{cs}$ could have been kept if a different definition ψ_{D2} was used, which results in $\psi_{D2} = 0$ at the critical state as shown in Eq. (14). Eq. (14) is obviously equivalent to Eq. (9) with state parameter form $\psi_{F3} = ln(e/e_{cs})$ and as such only the form ψ_{F3} is taken forward in the sequel.

$$\psi_{D2} = sign(\ln(\psi_{F2}))|\ln(\psi_{F2})|^w \tag{14}$$

3.3 LCSI and CSL functions

This section outlines how the functions that describe the available LCSI curves and the CSL were produced. Each LCSI curve was linked to the CSL through a plausible state parameter form, $\psi_{F1} = e - e_{cs}$ or $\psi_{F3} = ln\left(\frac{e_\zeta}{e_{cs}}\right)$. The function proposed by Bolton [8] and given in Eq. (15) was chosen to describe the CSL in $e - p'$ space, with $e_{max} = 0.782$ and $e_{min} = 0.538$ for Congleton sand experimentally obtained and parameters Q and R left to be defined. Using Eq. (15) ensured that the proposed CSL would remain below e_{max}.

$$e_{cs} = e_{max} - \frac{(e_{max} - e_{min})R}{Q - ln(p')} \tag{15}$$

Each LCSI curve was then expressed using the CSL function and the selected state parameter form (Eq. 16 or 17). Note that the experimental data give known pairs of (p', e_ζ).

$$\begin{aligned} &Form\ 1: \\ &e_\zeta = \psi_{F1,\zeta} + \left[e_{max} - \frac{(e_{max} - e_{min})R}{Q - ln(p')}\right] \\ &\quad = sign\left(\psi_{D1,\zeta}\right)\left|\psi_{D1,\zeta}\right|^{1/w} + e_{cs} \end{aligned} \tag{16}$$

$$\begin{aligned} &Form\ 3: \\ &e_\zeta = exp(\psi_{F3,\zeta}) \cdot \left[e_{max} - \frac{(e_{max} - e_{min})R}{Q - ln(p')}\right] \\ &\quad = exp(sign\left(\psi_{D3,\zeta}\right)\left|\psi_{D3,\zeta}\right|^{1/w}) \cdot e_{cs} \end{aligned} \tag{17}$$

Taking the (p', e_ζ) points of the reference $\zeta = -20\%$ set and the $\zeta = -30\%$ and $\zeta = -40\%$ sets translated to the reference through the Ω constants of Table 4, a curve fitting exercise for Eq. (16) ($\psi_{F1} = e - e_{cs}$) gave the values of $Q = 9.885$, $R = 0.685$ and $\psi_{F1,-20\%} = -0.0577$. Equivalently, using Eq. (17) ($\psi_{F3} = ln\left(\frac{e_\zeta}{e_{cs}}\right)$) gave $Q = 9.727$, $R = 0.707$ and $\psi_{F3,-20\%} = -0.0744$. A high value of parameter Q (~ 10) is indicative of the sand's mineralogy and according to Bolton [8] suggests a high silica content, as is indeed the case for Congleton sand. The value of R is typically around 1 for clean sands, with $R < 1$ reported before for silica sands, e.g. Kamai and Boulanger [21], Kassas et al. [22].

Thus expressions were produced to describe the CSL and the LCSI for $\zeta = -20\%$. The remaining LCSI curves were obtained using the constant Ω values of Table 4. The curves and their corresponding expressions are given in Fig. 7a for $\psi_{F1} = e - e_{cs}$ and Fig. 7b for $\psi_{F3} = ln\left(\frac{e_\zeta}{e_{cs}}\right)$. The values of $\psi_{F,\zeta}$ for each state parameter form are shown in Table 5. The tests from Table 2 are also plotted in $e - p'$ space in Fig. 8 along with the CSL determined in this study for both state parameter forms, which confirms that none of the tests attained critical state.

The two produced expressions for CSL are very similar until about $p' = 3000$ kPa, after which the curve corresponding to $\psi_{F3} = ln\left(\frac{e_\zeta}{e_{cs}}\right)$ becomes steeper. As mentioned before, a clearer distinction between the two state parameter forms could be made if LCSI points for each coupling ratio were obtained for the higher stresses where the curves become steeper. Though this is possible for some sands (e.g., Hostun sand in Dilip and Adamidis [13]), for the Congleton sand used here it would lead to mean effective stresses beyond the limits of the equipment and instrumentation used, and beyond the range of interest for most geotechnical applications.

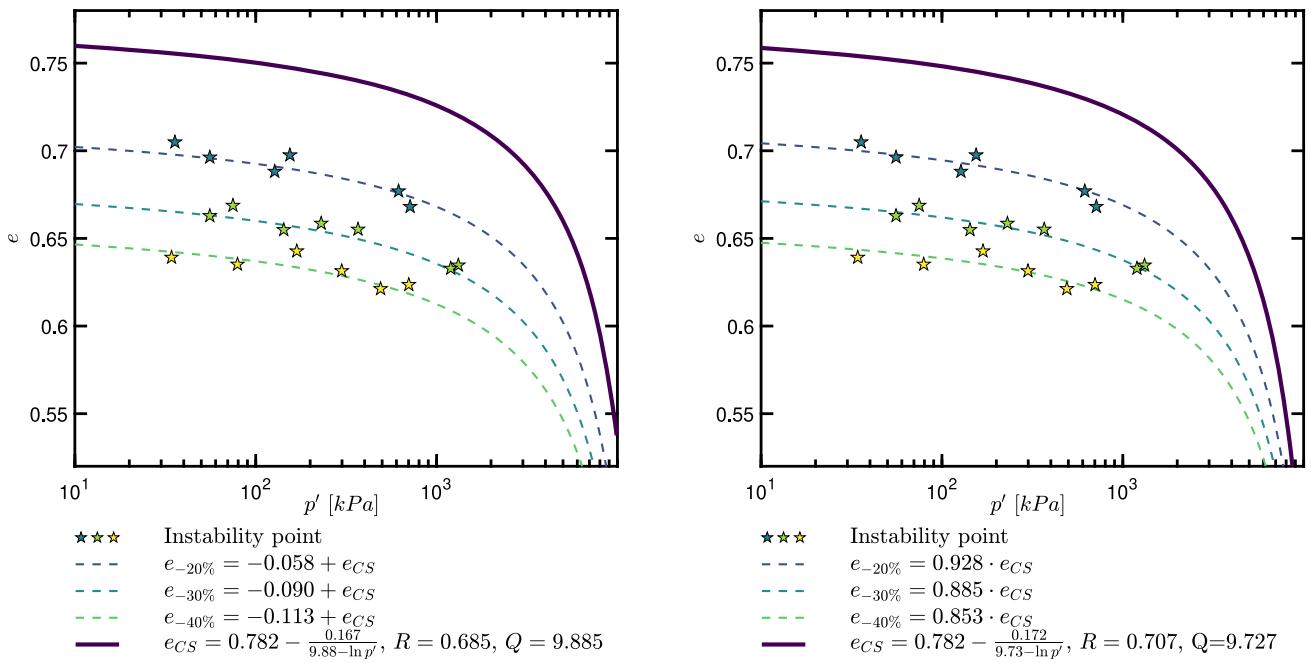

Fig. 7 Critical state line for Congleton sand for state parameter form (**a**) $\psi_{F1} = e - e_{cs}$ (left) and (**b**) $\psi_{F3} = ln\left(\frac{e_c}{e_{cs}}\right)$ (right)

Table 5 Values for state parameter forms $\psi_{F,\zeta}$ for Eqs. (10) and (13), corresponding to each inflow rate ζ

Inflow Rate	Form 1	$\psi_{F1,\zeta}$ Value	Form 3	$\psi_{F3,\zeta}$ Value
$\zeta = -20\%$	$\psi_{F1,-20\%} = e_{-20\%} - e_{cs}$	−0.0577	$\psi_{F3,-20\%} = ln(e_{-20\%}/e_{cs})$	−0.0744
$\zeta = -30\%$	$\psi_{F1,-30\%} = e_{-30\%} - e_{cs}$	−0.0903	$\psi_{F3,-30\%} = ln(e_{-30\%}/e_{cs})$	−0.1225
$\zeta = -40\%$	$\psi_{F1,-40\%} = e_{-40\%} - e_{cs}$	−0.1133	$\psi_{F3,-40\%} = ln(e_{-40\%}/e_{cs})$	−0.1584

3.4 Validation of the proposed methodology

In this section a validation exercise of the proposed methodology is presented for Hostun sand. The coupled shear-volumetric strain monotonic compression tests conducted by Dilip and Adamidis [13] were used to predict the CSL following the steps outlined in the previous sections. The relevant LCSI sets of points (post-phase transformation and post-peak stress ratio), determined using Hill's criterion [17] by Dilip and Adamidis [13] are listed in Table 6. State parameter forms ψ_{F1} (Eq. 10 and corresponding to state parameter definition of Eq. (9)) and ψ_{F2} (Eq. 11 and corresponding to state parameter definition of Eq. (14)) were examined following Section 3.2.

The assessment for the Ω constants for the two state parameter forms was conducted by selecting the LCSI point set corresponding to $\zeta = -15\%$ as the reference and translating the other two LCSI sets of points to the reference. Figure 9a shows the vertically translated points for form 1 of each LCSI set $'j'$ ($\zeta = -5\%$ and -10%) in $e - p'$ space to the reference set $'i'$ ($\zeta = -15\%$) using $\Omega_{1,i|j}$ (Eq. 10). Similarly, Fig. 9b shows the LCSI point sets for $'j'$

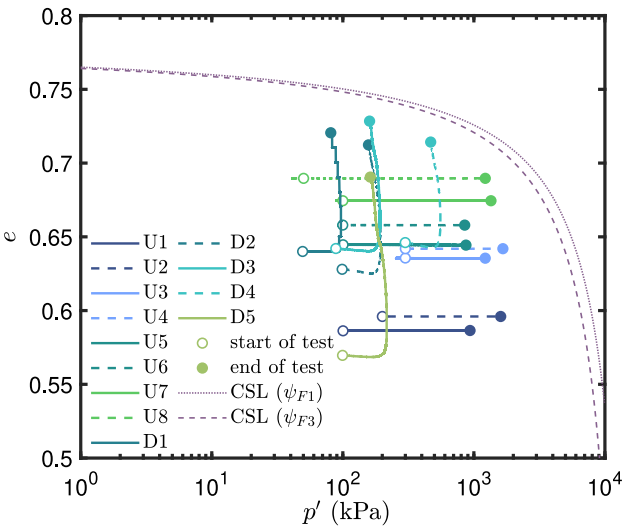

Fig. 8 Undrained and drained triaxial compression test paths for Congleton sand from Table 2 in $e - p'$ space where none of the tests reached the critical state line (CSL); predicted CSL shown for state parameter forms $\psi_{F1} = e - e_{cs}$ and $\psi_{F3} = ln(e/e_{cs})$

Table 6 LCSI instability points under three strain coupling ratios for Hostun sand from Dilip and Adamidis [13]

Test ID[a]	$p'_{INST}{}^{b}$	$e_{INST}{}^{b}$
ICPDMC/0.758/300/-5	963.9	0.774
ICPDMC/0.800/100/-5	459	0.819
ICPDMC/0.825/60/-5	297	0.846
ICPDMC/0.842/20/-5	191.4	0.861
ICPDMC/0.722/300/-10	1015.9	0.744
ICPDMC/0.748/250/-10	738.3	0.773
ICPDMC/0.818/80/-10	105.7	0.840
ICPDMC/0.828/30/-10	78.4	0.853
ICPDMC/0.714/300/-15	927.6	0.742
ICPDMC/0.737/250/-15	635.7	0.768
ICPDMC/0.763/100/-15	385.4	0.793
ICPDMC/0.804/50/-15	81.2	0.829

[a](1) type of consolidation: IC for isotropic consolidation; (2) type of drainage: PD for partially drained; (3)type of loading: MC for monotonic compression; (4) void ratio after consolidation; (5) mean effective stress after consolidation; and (6) coupled strain ratio during the shearing stage, $\zeta = \dot{\epsilon_v}/\dot{\epsilon_1}$, in percentage. [b]INST: Instability Point

Table 7 Values for Constants Ω_1 (based on state parameter form of Eq. (10)) and Ω_2 (based on state parameter form of Eq. (11)) resulting in the minimum mean of moving standard deviation for Hostun sand

Reference set	Constant	Definition	Value
$\zeta = -15\%$	$\Omega_{1,-15\%\|-5\%}$	$e_{-15\%} - e_{-5\%}$	−0.0414
$\zeta = -15\%$	$\Omega_{1,-15\%\|-10\%}$	$e_{-15\%} - e_{-10\%}$	−0.0187
		Mean of moving σ	0.0176
$\zeta = -15\%$	$\Omega_{2,-15\%\|-5\%}$	$e_{-15\%}/e_{-5\%}$	0.9485
$\zeta = -15\%$	$\Omega_{2,-15\%\|-10\%}$	$e_{-15\%}/e_{-10\%}$	0.9745
		Mean of moving σ	0.0171

($\zeta = -5\%$ and -10%) moved to the reference 'i' ($\zeta = -15\%$) in $e - p'$ space by a void ratio multiplication constant $\Omega_{2,i|j}$ (Eq. 11) for form 2. The Ω constants listed in Table 7 minimize the scatter of data points in $e - p'$ space, computed through the mean of the moving standard deviation of e across p', as illustrated in Fig. 10.

The state parameter form 2 (Eq. 11) was considered appropriate for the examined data, as it resulted in the minimum mean of the moving standard deviation of e (Table 7). Using the state parameter form 2 (e/ecs), the parameters of Bolton's CSL equation were determined, using the instability points for $\zeta = -15\%$ and the translated instability points for $\zeta = -5\%$ and $\zeta = -10\%$, as shown in Fig. 9b. The best-fit with $R^2 = 0.99$ was obtained using $Q = 8.5$, $R = 0.83$ and $e_{-15\%}/e_{cs} = 0.898$. The obtained Q and R parameters for the critical state can be compared to those determined directly, using undrained and drained monotonic compression tests, by Dilip and Adamidis [13]: $Q = 8.3$ and $R = 0.73$. For $\zeta = -15\%$ and with a known CSL, a value of $e_{-15\%}/e_{cs} = 0.897$ was calculated. The back-calculated and the directly obtained CSL for Hostun sand are shown in Fig. 11. As seen from the figure, the proposed methodology using proportional strain paths can accurately locate the CSL in $e - p'$ space.

3.5 State parameter definition

The investigation up to the previous section is sufficient to derive an expression for the CSL through coupled strain

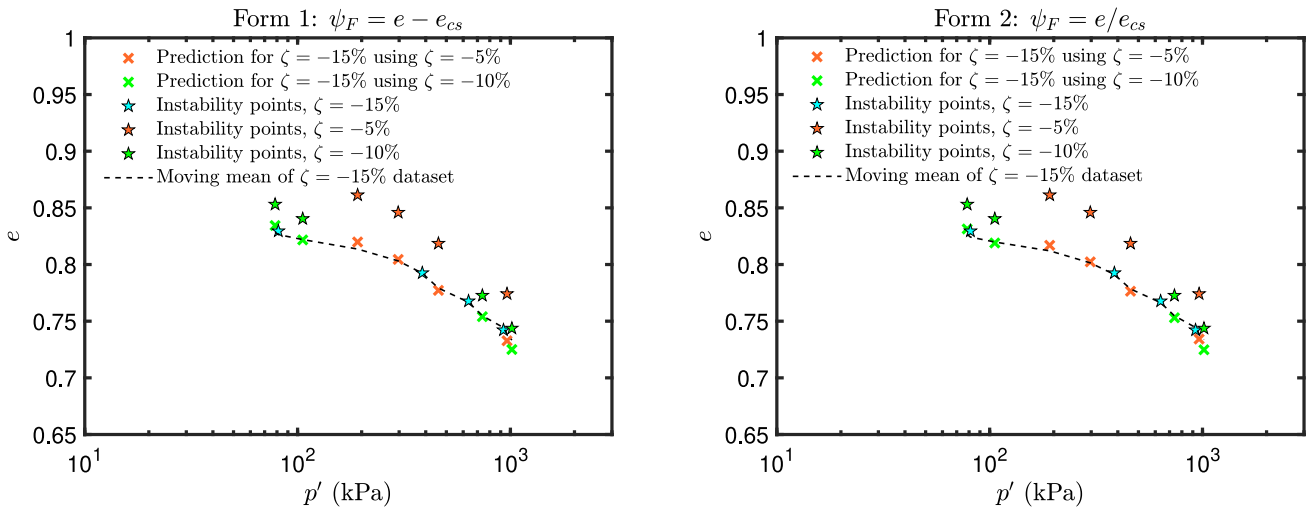

Fig. 9 Assessment of state parameter forms, **a** Form 1: $\psi_{F1,\zeta} = e_\zeta - e_{cs}$ and **b** Form 2: $\psi_{F2,\zeta} = \frac{e_\zeta}{e_{cs}}$, through transferring LCSI points for $\zeta = -5\%$ and -10% to the $\zeta = -15\%$ LCSI curve for Hostun sand

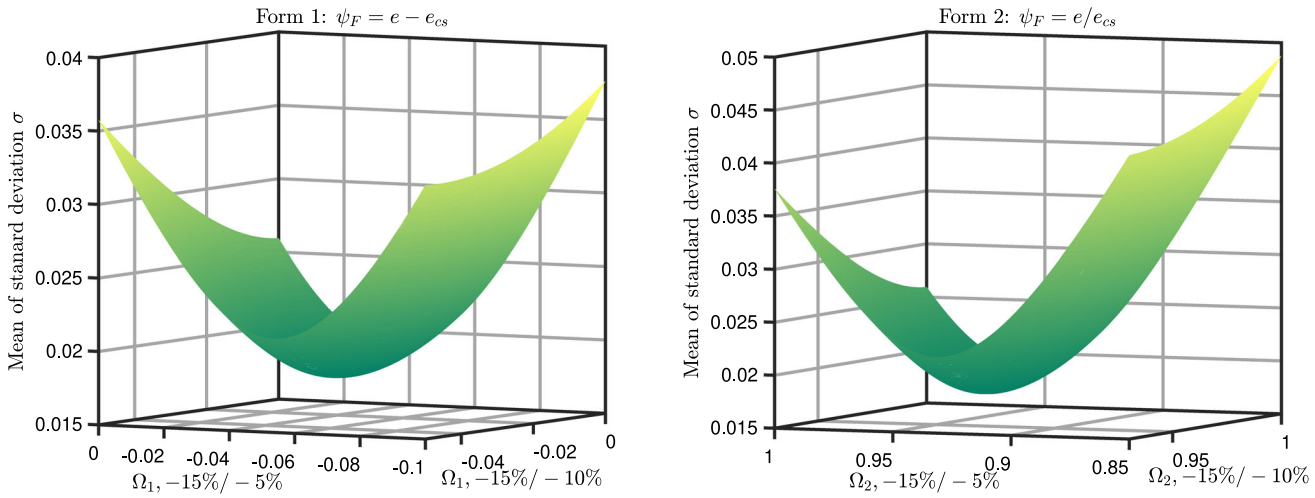

Fig. 10 Mean of moving (5 point) standard deviation of all experimentally obtained points translated to the reference $\zeta = -15\%$ LCSI curve based on state parameter forms **a** Form 1: $\psi_{F1,\zeta} = e_\zeta - e_{cs}$ and **b** Form 2: $\psi_{F2,\zeta} = \frac{e_\zeta}{e_{cs}}$ for Hostun sand

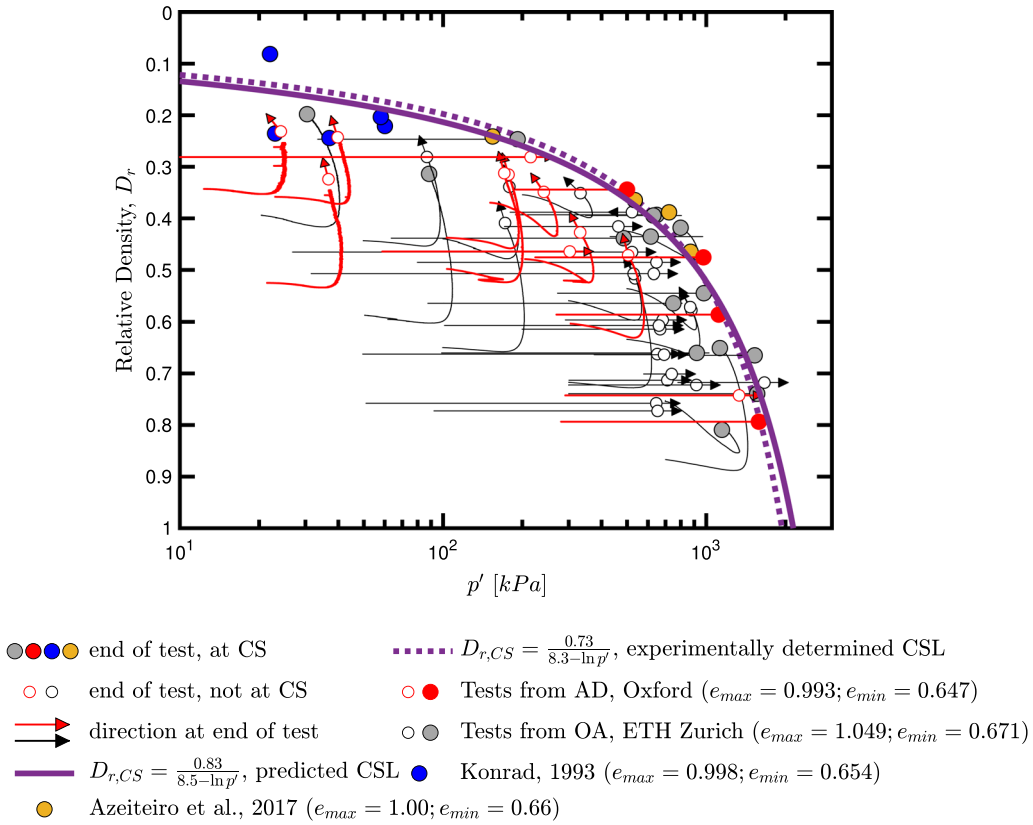

Fig. 11 Experimentally determined CSL of Hostun sand from Dilip and Adamidis [13] in $e - p'$ and predicted CSL for Hostun sand determined using the methodology in this study

compression tests. Though at this point appropriate state parameter forms ψ_F have been identified, a definition of the state parameter ψ_D that satisfies Eq. (8) numerically for all experimentally obtained LCSI curves remains unknown. If the use of a SANISAND model is intended, then the final step in the CSL determination, necessary for model calibration, is the selection of a state parameter definition ψ_D. Here, returning to the results on Congleton sand, the proposed definition in Eq. (9) is investigated for the two state parameter forms considered in the previous section,

$\psi_{F1} = e - e_{cs}$ and $\psi_{F3} = ln\left(\frac{e}{e_{cs}}\right)$. Following Eq. (8), ψ_D must be linearly related to $\Lambda = \frac{3\zeta}{3-\zeta}$.

Note that for water inflow conditions where $\Lambda < 0$, $\psi_D < 0 \Rightarrow \psi_F < 0$, indicating that the LCSI curves fall below the CSL in $e - p'$ space. With increasing rates of inflow (increasing magnitudes of Λ), ψ_D increases in magnitude monotonically. The experimental LCSI curves (Fig. 7) indicate that as Λ increases in magnitude, so do the selected forms ψ_F, so that a positive exponent w in Eq. (9) is needed to produce the required linear dependency of ψ_D on Λ.

The values of the state parameter forms ψ_{F1} and ψ_{F3} listed in Table 5 were used for the state parameter definition ψ_D of Eq. (9) and the produced ψ_D values were substituted in Eq. (8), to obtain the following relation for $C = A_d(k^d + k^b)$ at each strain coupling ratio ζ_i:

$$\begin{aligned} &At\ \zeta_i,\ \ C \cdot \psi_{D,\zeta_i} = \frac{3\zeta_i}{3-\zeta_i} = \Lambda_i \\ &\Rightarrow Form\ 1 : C \cdot (-\psi_{F1,\zeta_i})^w = -\Lambda_i \\ &\Rightarrow Form\ 3 : C \cdot (-\psi_{F3,\zeta_i})^w = -\Lambda_i \end{aligned} \tag{18}$$

For each state parameter form ψ_F, a positive coefficient C and a positive exponent w were obtained through curve fitting of Eq. (18) using the three available points of $(\psi_{F,\zeta_i}, \Lambda_i)$, corresponding to the three strain coupling ratios examined. Figure 12 depicts this process of relating Λ to the available ψ_F values and gives the calculated C and w values for the two state parameter forms considered. For both forms ψ_F examined, the coefficient of determination for the fitted ψ_D was $R^2 = 0.993$. The more experimentally obtained LCSI curves available, the more points can be added to the graphs of Fig. 12, allowing further scrutiny on the definition of ψ_D. For Eq. (9), assumed to apply here, further points would lead to a more accurate exponent w.

Thus, the state parameter definition needed for the constitutive model formulation and calibration (Eq. 9) was fully defined for both state parameter forms. At the end of this investigation, two state parameter definitions $\psi_{D1} = sign(e - e_{cs})|(e - e_{cs})|^{0.95}$ and $\psi_{D3} = sign(ln\left(\frac{e}{e_{cs}}\right))|ln\left(\frac{e}{e_{cs}}\right)|^{0.85}$ were deemed equally appropriate for the available experimental data. In the sequel, ψ_{D3} is used, to maintain consistency with Dilip and Adamidis [13].

4 Model calibration

This section examines the possibility of using the coupled strain tests noted in Table 3 to determine additional SANISAND 2008 model parameters. However, not all calibration parameters can be directly derived from these tests. Undrained experiments presented in Table 2 are used additionally, as required to achieve a model calibration for Congleton sand that can be used to numerically capture triaxial compression experiments.

4.1 Elastic shear modulus

The small-strain shear modulus, G_{max}, is one of the two elasticity parameters required for calibration. As it cannot be directly obtained from the coupled-strain tests presented up to now, additional, bender element tests were conducted. The sample preparation process remained as described for the coupled strain tests. Specimens were prepared at three void ratio values and each was isotropically consolidated in steps, to six levels of mean effective

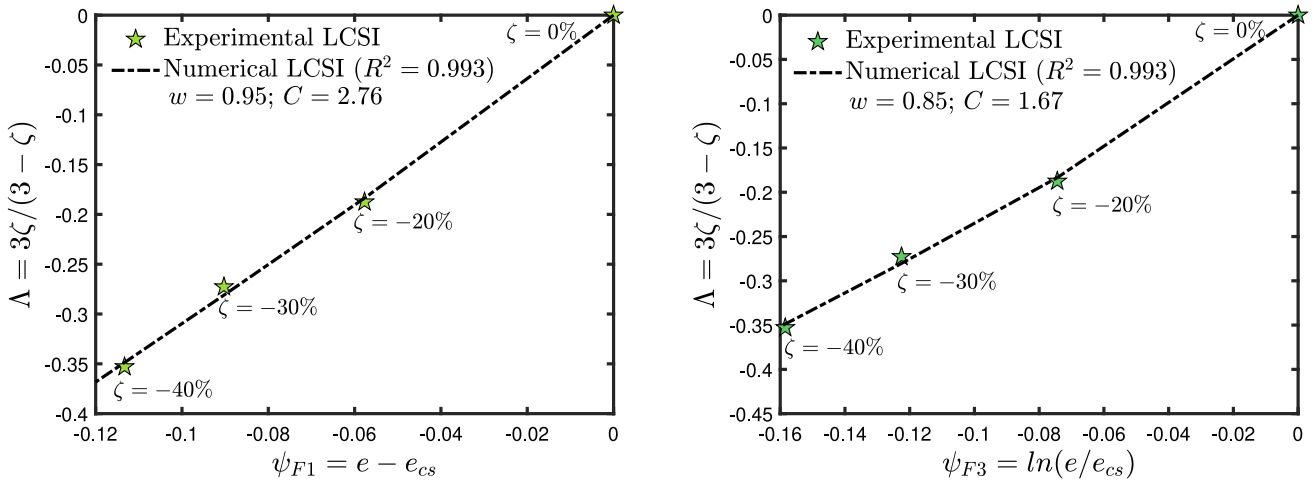

Fig. 12 Determination of parameters w and $C = A_d(k^d + k^b)$ using **a** Form 1: $\psi_{F1,\zeta} = e_\zeta - e_{cs}$ and **b** Form 3: $\psi_{F3,\zeta} = ln(e_\zeta/e_{cs})$

stress, with measurements on shear wave velocity made at each step. The travel time for the shear wave was determined using the peak-to-peak method between input and output signal. A summary of the bender element test results is presented in Table 8.

The corresponding expression for G_{max} is noted in Eq. (19) and shown in Fig. 13.

$$G_{max} = G_0 P_{at} \frac{(2.97-e)^2}{1+e} \left(\frac{p'}{P_{at}}\right)^{0.5} \quad where\ G_0 = 260 \tag{19}$$

The value of the small-strain shear modulus G_{max} as obtained from bender element tests has been reported in literature to overestimate by a factor of 2 to 4 the shear modulus required within bounding surface plasticity models of the SANISAND family in order to adequately capture triaxial compression tests at low to medium strain levels [3, 32, 33]. Dilip and Adamidis [13] used a value of $G_{max}/3$ to calibrate the SANISAND 2008 model in order to obtain good agreement with triaxial compression experiments for Hostun sand. A factor of two was applied here for Congleton sand, with the final expression adopted for the shear modulus used within SANISAND 2008 shown in Eq. (20).

Table 8 Results of bender element tests on Congleton sand using first peak for travel time estimation

Initial D_r [a]	p' [a]	e [a]	t [b]	V_s [b]	G_{max} [b]
30%	24.7	0.745	1.000	130.4	32.9
30%	49.5	0.743	0.828	160	49.5
30%	99.7	0.740	0.680	194.8	73.5
30%	199.7	0.737	0.562	235.3	107.3
30%	399.8	0.732	0.470	281.3	153.6
30%	599.6	0.729	0.423	311.9	189.0
50%	24.6	0.704	0.981	135.5	35.9
50%	49.4	0.702	0.801	165.9	53.9
50%	99.7	0.699	0.661	201.0	79.2
50%	199.7	0.696	0.548	242.1	114.9
50%	399.6	0.692	0.458	289.3	164.4
50%	599.9	0.689	0.415	319.4	200.5
70%	24.2	0.683	0.972	137.4	37.2
70%	49.3	0.681	0.792	168.5	55.9
70%	99.3	0.678	0.653	204.3	82.3
70%	199.2	0.675	0.543	245.3	118.7
70%	399.4	0.671	0.453	293.7	170.3
70%	599.5	0.669	0.408	326.1	210.3

[a]Post consolidation values. [b](1)t: travel time using first peak in ms; (2)V_s: shear wave velocity in m/s; (3)G_{max}: elastic shear modulus in MPa

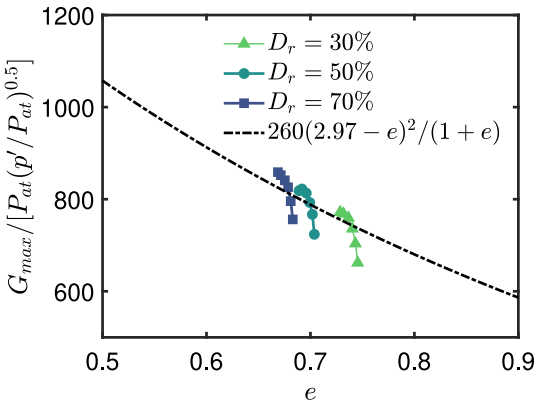

Fig. 13 Calibration of G_{max} using bender element tests on isotropically consolidated Congleton sand

$$G_{max} = G_0 P_{at} \frac{(2.97-e)^2}{1+e} \left(\frac{p'}{P_{at}}\right)^{0.5} \quad where\ G_0 = 130 \tag{20}$$

4.2 Elastic bulk modulus

The elastic bulk modulus, K can be obtained either directly from isotropic unloading experiments or indirectly from the elastic shear modulus and Poisson's ratio [41]. In this study, K was obtained from the elastic shear modulus G (Eq. 20) and Poisson's ratio v, as shown in Eq. (21). The typical value of $v = 0.05$ was used based on Dafalias and Manzari [12].

$$K = \frac{2(1+v)}{3(1-2v)} G \tag{21}$$

4.3 Bounding surface

The bounding surface parameter can either be defined following an exponential or a linear evolution of the bounding stress ratio, M^b, with the state parameter, ψ_D. Parameter n^b in Eq. (22) corresponds to an exponential evolution, whereas parameter k^b corresponds to a linear evolution. The latter is selected in this study as it produces a linear LCSI equation (Eq. 8) which facilitates calculations. Values for M^b can be obtained experimentally from peak stress ratio states (PSRS), η_{PSRS}. Such values from the coupled strain tests listed in Table 3 are plotted against their corresponding state parameter, ψ_D^b in Fig. 14. The slope of the fitted line gives the k^b value, while the ordinate of the fitted line at $\psi_D = 0$ can be used to infer the critical state stress ratio, M_c.

$$M^b = M_c exp(-n^b \psi_D) \ or \ M^b = M_c - k^b \psi_D \tag{22}$$

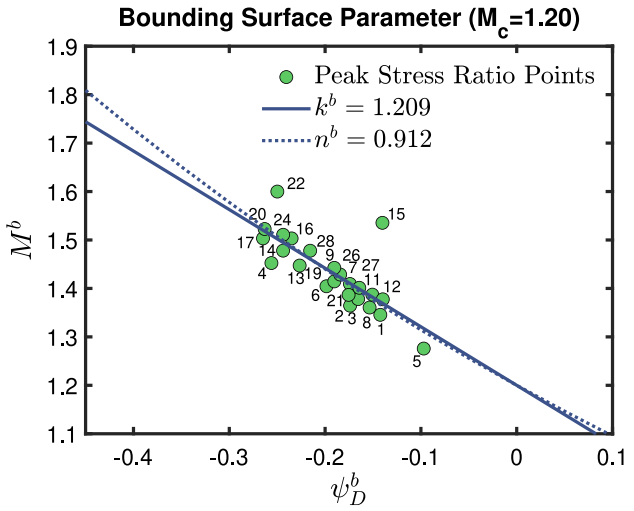

Fig. 14 Calibration of constants k^b and n^b (Eq. 22) for Congleton sand using the results of coupled strain monotonic compression tests

4.4 Dilatancy surface

To obtain the dilatancy surface parameter, the phase transformation state (PTS), i.e., the point of transition from contraction to dilation ($D = 0$) must be detected. This can be easily done in undrained tests, where $D = 0$ when $\dot{p'} = 0$. However, coupled strain tests impose nonzero volumetric strain increments, $\dot{\epsilon_v} \neq 0$, so that the point of $\dot{\epsilon_v}^p = 0$ cannot be directly deduced from the vanishing of $\dot{\epsilon_v}^e$. Instead, the elastic parameters must be known to locate the PTS, which introduces uncertainty. Thus, the series of undrained monotonic compression tests on Congleton sand presented in Table 2 were used to capture phase transformation points, as summarized in Table 9.

The dilatancy surface parameter can either be defined as n^d following an exponential evolution of the dilatancy surface stress ratio, M^d, with ψ_D, or as k^d if a linear evolution is preferred (Eq. 23). Here, a linear evolution was chosen, to match the assumption made for the bounding surface. Values of M^d obtained from the undrained compression tests at the phase transformation stress ratio, η_{PTS}, are plotted against their corresponding state parameter, ψ_D^d, in Fig. 15. With the value of M_c calculated as described in the previous section, the slope of the best-fit line gives the k^d value. It is worth noting that despite using undrained compression tests, scatter is still present in the data.

$$M^d = M_c exp(n^d \psi_D) \;\; or \;\; M^d = M_c + k^d \psi_D \tag{23}$$

Table 9 Results of undrained monotonic triaxial tests on Congleton sand

Test ID[a]	${e_{PTS}}^b$	${p'_{PTS}}^b$	${\eta_{PTS}}^b$
ICUMC/0.586/100 (U1)	0.586	105.7	1.14
ICUMC/0.596/200 (U2)	0.596	199.0	1.13
ICUMC/0.636/300 (U3)	0.636	260.6	1.14
ICUMC/0.642/300 (U4)	0.642	297.1	1.11
ICUMC/0.645/100 (U5)	0.645	91.5	1.08
ICUMC/0.658/100 (U6)	0.658	94.1	1.06
ICUMC/0.674/100 (U7)	0.674	91.7	1.06
ICUMC/0.690/50 (U8)	0.690	41.3	1.08

[a](1)type of consolidation: IC for isotropic consolidation; (2)type of drainage: U for undrained; (3)type of loading: MC for monotonic compression; (4)void ratio immediately after consolidation; (5)mean effective stress immediately after consolidation. [b]PTS: Phase Transformation State

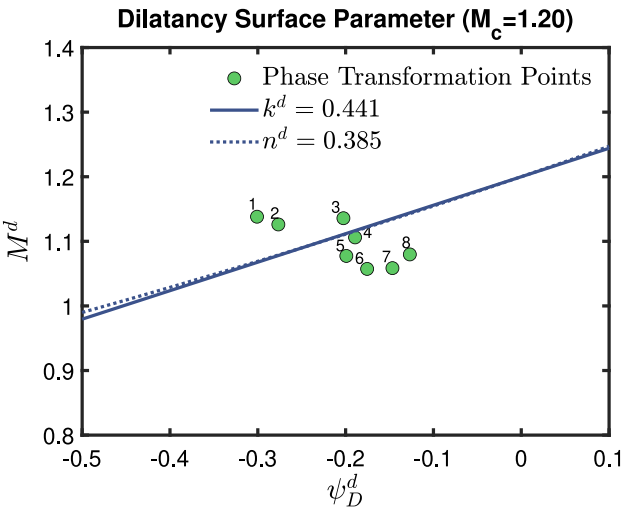

Fig. 15 Calibration of constants k^d and n^d (Eq. 23) for Congleton sand using the results of undrained monotonic compression tests

4.5 Fitting parameters

The dilatancy constant A_d (Eq. 4) is typically determined from stress-dilatancy curves of drained tests [41]. However, in this case, Eq. (8) was used to evaluate parameter A_d, eliminating the need for additional experiments. Figure 12b shows a plot of the right-hand side of Eq. (8), varying with the state parameter, ψ_D ($\psi_D = f(\psi_F)$ per Eq. (9) with $w = 0.85$). The slope of the best-fit gives the value of the coefficient $C = A_d(k^d + k^b) = 1.67$. With the bounding surface parameter $k^b = 1.209$ and the dilatancy surface parameter $k^d = 0.441$ as calculated earlier, a value of the dilatancy parameter, $A_d = 1.012$ was determined.

Parameters h_0 and c_h were selected by trial-and-error, by fitting undrained triaxial test simulation results to experiments in $q - \epsilon_1$ space at low to medium strains, as in Taiebat et al. [42]. An exponential dependence on the void ratio [41] ensures positive values for h in Eq. (3) across the range of void ratios noted in Table 1. Figure 16 shows the chosen values of the parameters.

4.6 Compression parameters

The compression parameters are not included here as they are only applicable for a high confining pressure range, around $p' = 10 - 50$ MPa for siliceous sands [41], which is beyond the range of interest of this study.

5 Model performance

A summary of the selected SANISAND 2008 model parameters for Congleton sand are listed in Table 10. Parameter c, the ratio of the slope of the critical surface in triaxial extension to compression and parameter m, controlling the size of the elastic wedge, were taken from Dafalias and Manzari [12]. As discussed above, the shear modulus G was based on a reduced value of that measured through bender element tests and the bulk modulus K was obtained from the shear modulus G and a Poisson's ratio $v = 0.05$. Parameters M_c, R, Q, n^b or k^b, and A_d were directly obtained from the coupled strain compression tests used to infer the CSL. Parameters n^d or k^d, h_0, and c_h were obtained from undrained tests. This section includes the simulation results for the undrained and the coupled strain experimental tests on Congleton sand.

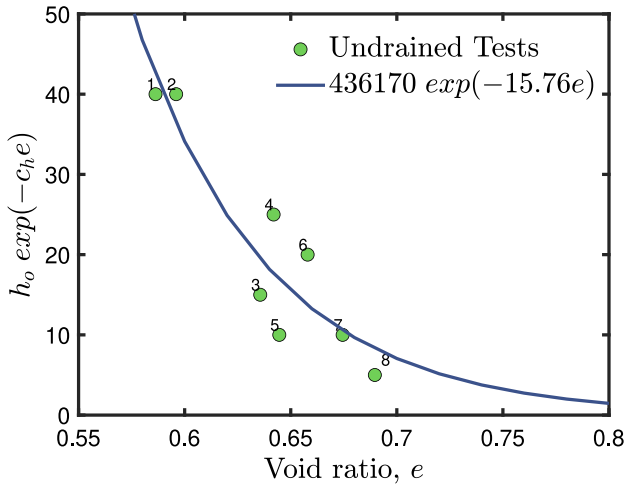

Fig. 16 Calibration of h_0 and c_h for Congleton sand using the results of undrained monotonic compression tests

Table 10 SANISAND model parameters for Congleton sand, refer Dilip and Adamidis [13] for other parameter definitions

Parameter	Values	Parameter	Values	Parameter	Values
G_0 (kPa)	130[(a)]	e_{max}	0.782	n^b	0.912
v	0.05[(b)]	e_{min}	0.538	k^b	1.209
M_c	1.20	R	0.707	h_0	436170[(c)]
α^c	1.19	Q	9.727	c_h	15.76[(c)]
m	0.01	n^d	0.385	A_d	1.012
c	0.71	k^d	0.441	P_{at} (kPa)	100

[(a)]Implemented in Eq. (20). [(b)]Implemented in Eq. (21). [(c)]Exponential function used, see Fig. 16

5.1 Undrained monotonic triaxial test simulations

A comparison between the numerical simulations and the experimental data for the undrained tests of Table 2 is shown in Fig. 17. The simulations adequately captured the undrained behaviour across the range of examined densities, both in terms of stress space paths and in terms of stress–strain behaviour.

5.2 Coupled strain triaxial compression test simulations

Using the calibration parameters for a linear evolution of bounding and dilatancy surfaces from Table 10, the proposed CSL form (Eq. 15) and the state parameter definition ψ_D, the coupled strain triaxial tests of Table 3 were numerically simulated using SANISAND 2008 [41]. The comparisons between simulation and experiments are shown in Figs. 18, 19, 20. The LCSI instability points of the simulations were detected using Hill's criterion (Eq. 6), similarly to the experimental data. Instability points are depicted in square markers for the numerical simulations and star markers for the experimental data. The simulated coupled strain paths were also plotted in $e - p'$ space in Figure 21 and compared to the experimental data.

Overall, the calibrated parameters allowed the model to capture the observed behaviour well, across all strain coupling ratios examined. Although the numerical instability points do not exactly match the experimental instability points, the stress paths in $q - p'$ space were adequately replicated. The effective stresses follow a similar path to undrained tests for medium-dense/dense sands, but before the CSL can be reached a reversal towards diminishing p' and q is observed. Initially, the soil accommodates the expansive volumetric strains. After the dilatancy has reached its minimum negative value and has

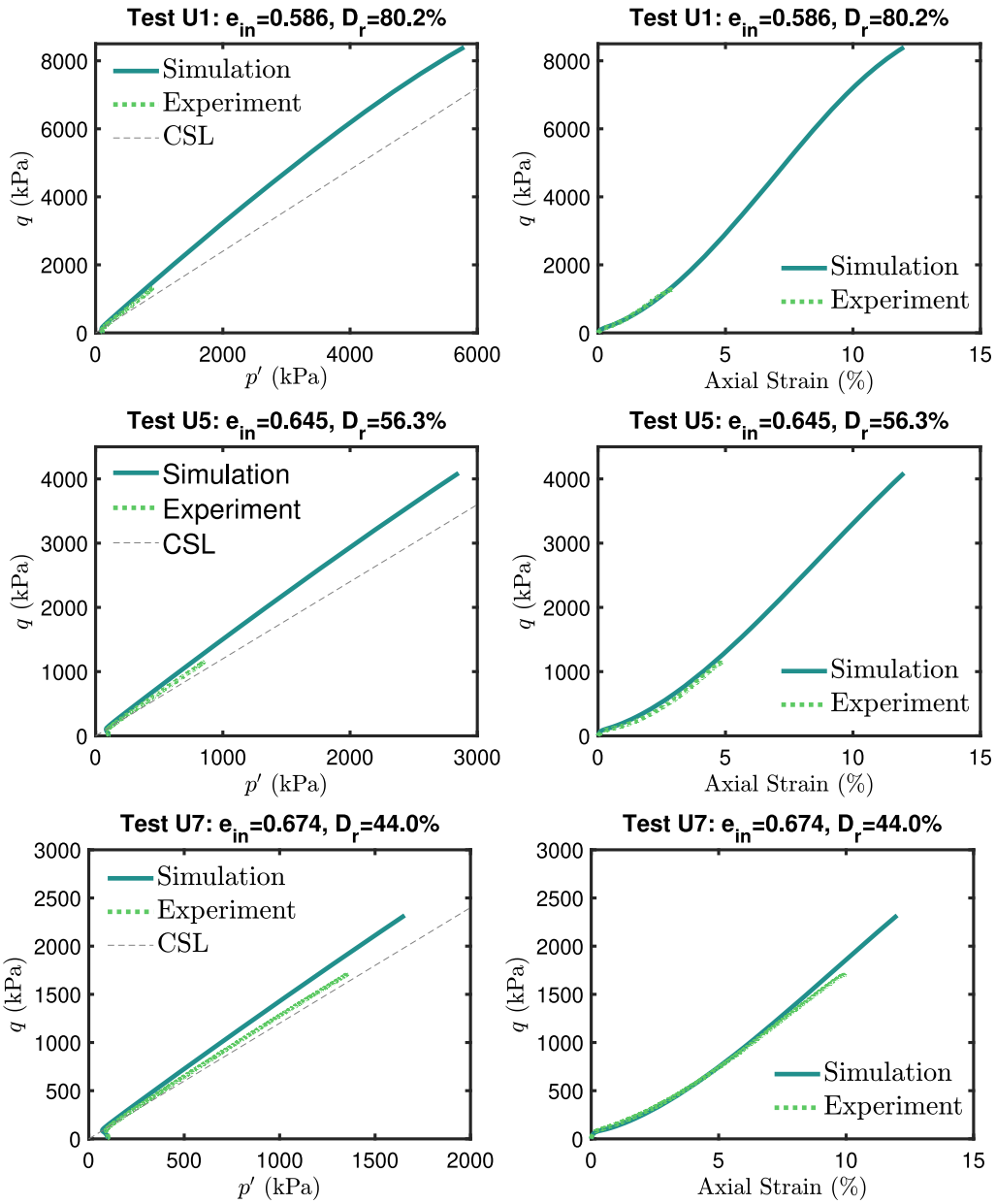

Fig. 17 Simulations of undrained monotonic triaxial compression tests on isotropically consolidated samples of Congleton sand and comparison with experimental test data

increased to match the imposed strain coupling ratio ($D = \Lambda < 0$), the soil is no longer able to sustain the continuous expansive volumetric strain and unloading takes place (reduction in p' and q). A drastic increase in void ratio and shear strain follows. In the $q - \epsilon_1$ plots, the peak deviator stresses and the instability points were detected at axial strains similar to the corresponding experimental values. The magnitude of the peak deviator stress was also overall captured well. An exception was the last experiment of Fig. 20, where larger than experimentally observed values of p' and q were reached. This is because for $\zeta = -40\%$ and to a lesser extent for $\zeta = -30\%$, experiments with low initial mean effective stress were less dilative than predicted by the simulations (Fig. 21).

Figure 21 presents results in $e - p'$ space and confirms that the numerically calculated and the experimentally observed LCSI curves (constant ψ_F or ψ_D) practically coincide. For instance, for $\zeta = -30\%$, the experimental constant ψ_D line is located at $e_{-30\%} = 0.885 e_{cs}$ (Fig. 7b), while as shown in Fig. 12b the power fit used in Eq. (8) predicts the constant ψ_D line at $e_{-30\%} = 0.888 e_{cs}$. For the other two strain coupling ratios, the predicted numerical LCSI is even closer to the experimental LCSI in Fig. 21, as also depicted in Fig. 12b. Across all coupling ratios, as

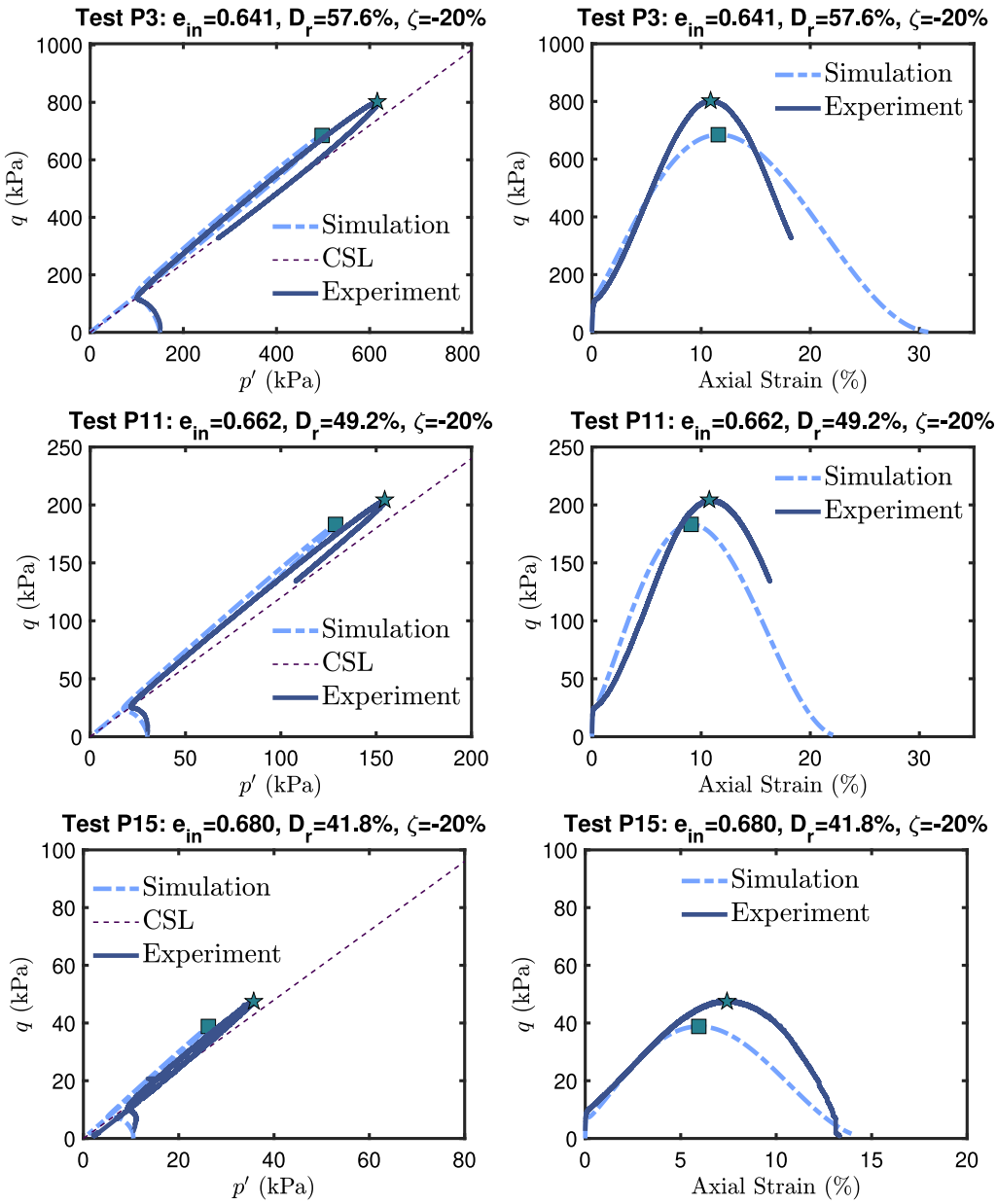

Fig. 18 Simulations of coupled strain monotonic triaxial compression tests under $\zeta = -20\%$ on isotropically consolidated samples of Congleton sand and comparison with experimental test data

already stated, experiments with $p' < 100$ kPa and $e < 0.65$ were less dilative than their corresponding simulations. On the contrary, simulations captured very well experiments with initial mean effective stress of $p' > 100$ kPa or $p' < 100$ kPa with $e > 0.65$. It is worth noting that the dilatancy surface parameter k^d was calibrated from undrained tests in Table 2, shown in Fig. 8, where all but one undrained tests had $p' > 100$ kPa, while the test capturing $p' < 100$ kPa was at a void ratio $e > 0.65$. Therefore, the calibration process of parameter k^d in Fig. 15 did not directly capture cases where phase transformation occurs at $p' < 100$ kPa and $e < 0.65$.

6 Conclusions

Locating the critical state line (CSL) through element tests can be a challenging or impossible task for some sands. This is often due to the excessive strains required to reach the critical state, which can be beyond what testing protocols allow, and which necessitate significant corrections that render result interpretation challenging. In addition, very dilative sands might require the application of loads that are beyond the limits of typical equipment or instrumentation, especially when considering high initial confining stresses. Further, undrained compression tests for

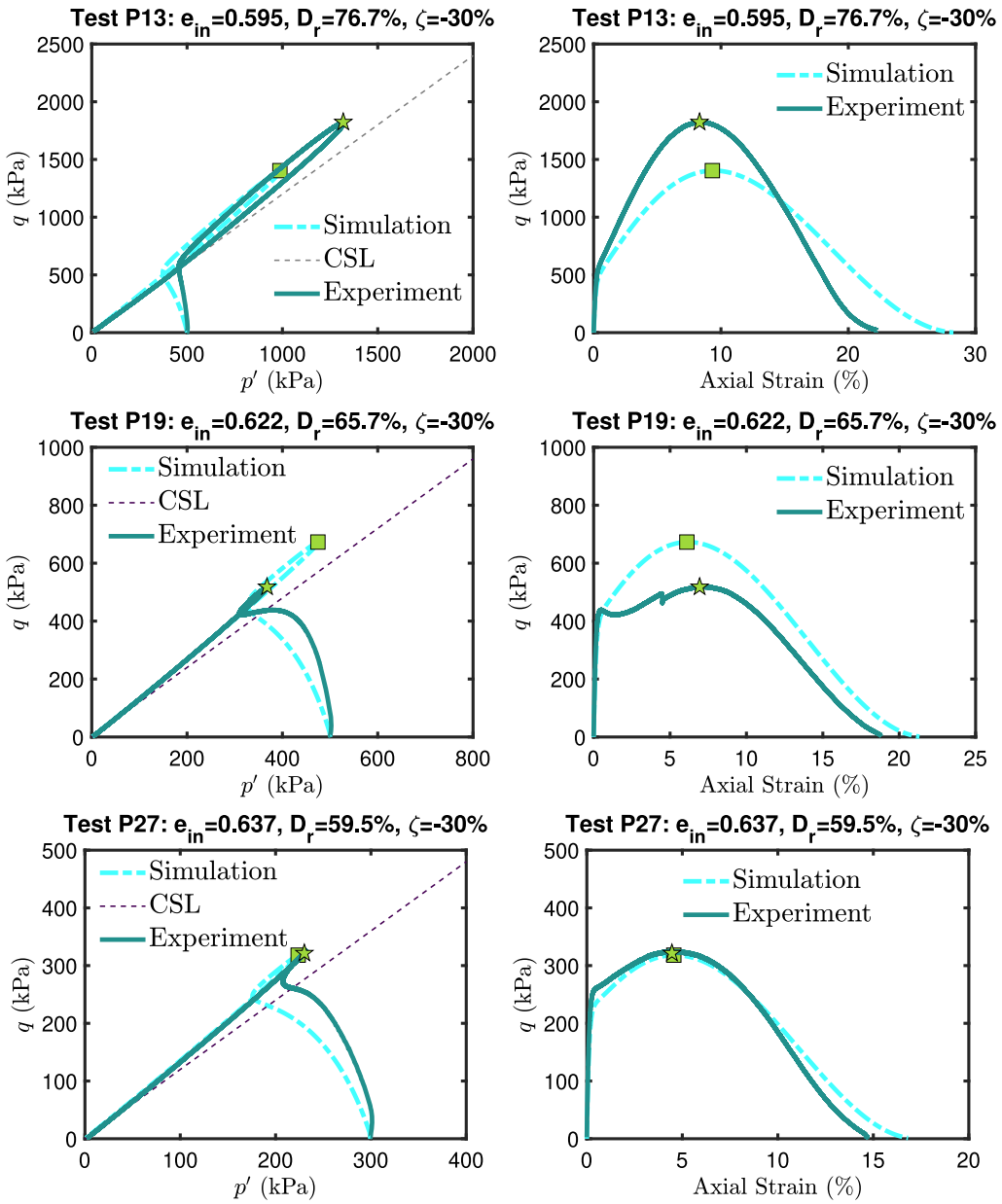

Fig. 19 Simulations of coupled strain monotonic triaxial compression tests under $\zeta = -30\%$ on isotropically consolidated samples of Congleton sand and comparison with experimental test data

dilative sands can quickly lead to negative pore water pressure and potential cavitation, which prohibits the specimen from reaching the critical state. Finally, scanning the entire density range with experiments is not possible for many sample preparation methods.

In this study, an alternative experimental approach to estimate the CSL is proposed, using coupled shear-volumetric strain triaxial compression experiments. These experiments do not require axial strains beyond the generally accepted threshold of 15%. The CSL is indirectly identified through the concept of the Locus of Constant State parameter Instability points (LCSI), as described within the context of bounding surface plasticity models of the SANISAND family by Dilip and Adamidis [13]. The proposed method requires triaxial compression tests where the volumetric strain increment is a constant fraction of the axial strain increment, conducted under different strain coupling ratios (ζ). Post-phase transformation and post-peak stress ratio instability points identified using Hill's criterion are first used to establish the LCSI for each ζ. The LCSI curves are then compared to identify an appropriate state parameter form. Using this form, equations for the LCSI and the CSL curves, as well as the corresponding state parameter definition can be derived. While three

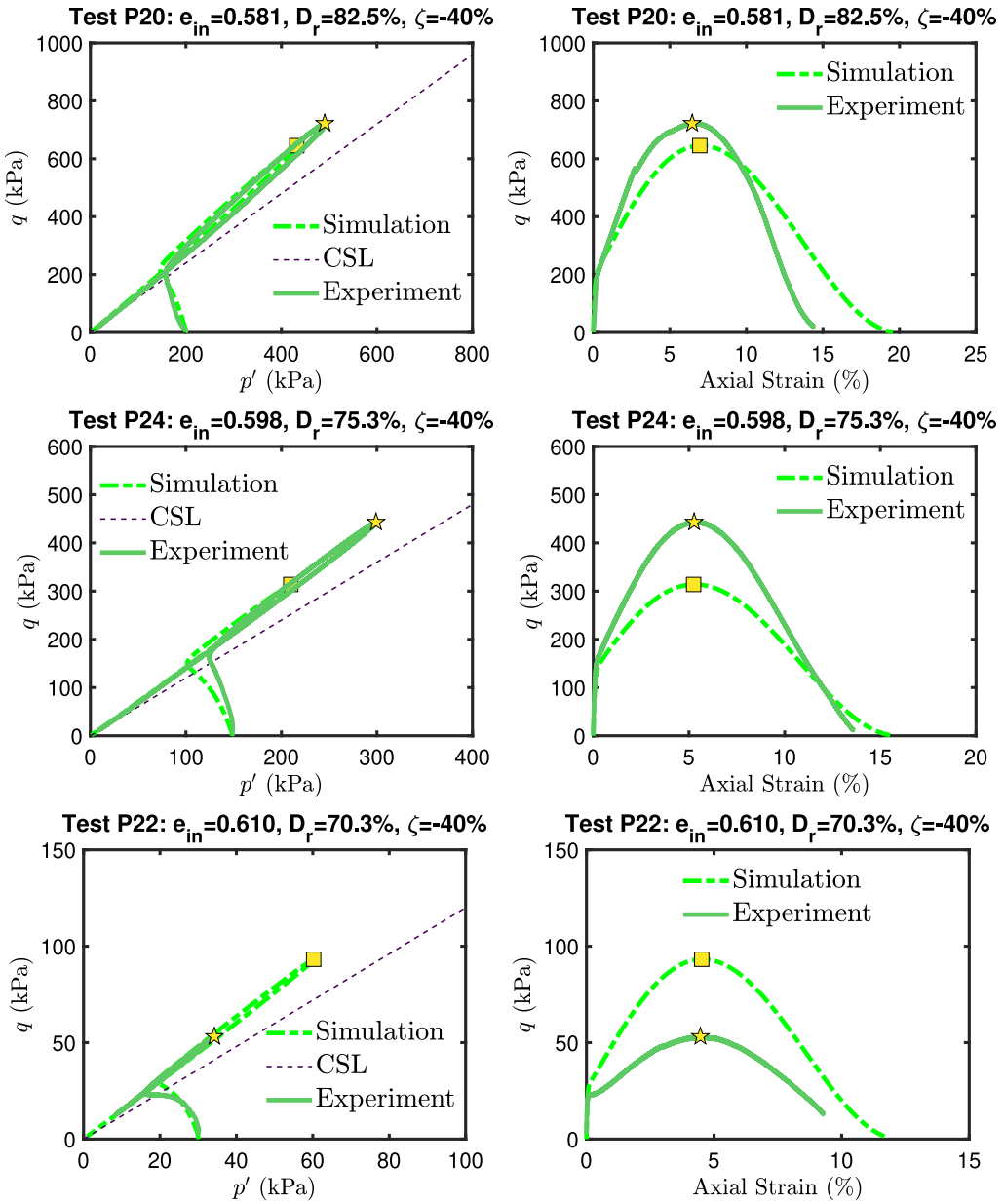

Fig. 20 Simulations of coupled strain monotonic triaxial compression tests under $\zeta = -40\%$ on isotropically consolidated samples of Congleton sand and comparison with experimental test data

coupling ratios ζ are sufficient for an estimate of the CSL, as shown here, more values of ζ could provide increased reliability regarding the identified state parameter definition and the proposed CSL.

The coupled strain triaxial compression tests performed to identify the CSL can further aid in the calibration of a SANISAND model. Here, the bounding surface parameters and the critical surface stress ratio were directly obtained through the peak stress ratio points captured in these tests. However, determining the dilatancy surface parameters by identifying points of phase transformation state (PTS) was less straightforward, as due to the imposed volumetric strain rate, $\dot{p'} \neq 0$ at PTS. Instead, additional undrained tests sheared to low strain levels were used to obtain phase transformation points. For the elastic shear modulus, bender element tests were used. The elastic bulk modulus was estimated based on the elastic shear modulus and a typical value for Poisson's ratio used in SANISAND models. Finally, no drained tests were required to determine the dilatancy constant A_d, which was calculated from the coupled strain tests using the equation of the LCSI. The hardening constants were calibrated using iterations, based

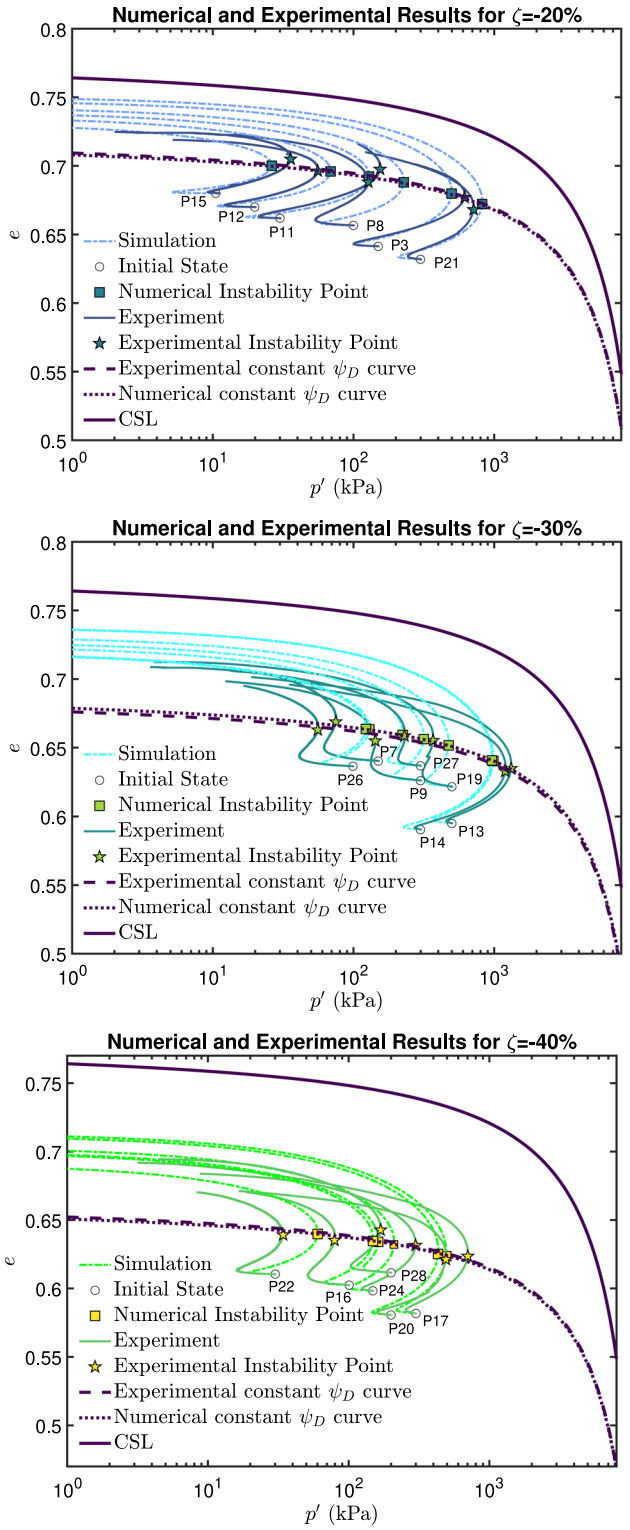

Fig. 21 Simulations of coupled strain monotonic triaxial compression tests on Congleton sand under $\zeta = -20\%$, -30% and -40% in $e - p'$ space and comparison with experimental test data

on the undrained compression results at low to medium strain. Overall, the use of the coupled strain triaxial compression tests eliminated the need for drained stress-dilatancy data and in general the need for any experiment that reaches large strains.

Congleton sand was used for the experiments presented throughout this paper, apart from a validation exercise on Hostun sand, and consequently a set of calibration parameters for monotonic modelling of Congleton sand within the SANISAND framework was produced. Congleton is a dilative sand for which we were unable to reach the critical state through conventional testing. With the derived CSL and the remaining SANISAND calibration parameters, a good replication of the experimental test paths was obtained for both the undrained and the coupled strain conditions.

It is worth noting that the method proposed in this paper to estimate the CSL, which is an inherent property of the soil, is based on the LCSI curve framework which was derived for SANISAND models. While no soil is bound to follow the SANISAND set of equations, the data of Dilip and Adamidis [13] show that the (known) CSL of Hostun sand can be accurately predicted through this method, while the data of this paper show that the estimated CSL for Congleton sand, when incorporated in numerical simulations, results in good predictions of observed behaviour.

Acknowledgements The first author would like to thank University College and the Department of Engineering Science for awarding her the Oxford-Ashton Memorial Graduate scholarship which funded her DPhil studies. The second author would like to thank the China Scholarship Council for supporting his visit to the University of Oxford.

Data Availability Data will be made available on request.

Declarations

Conflict of interest The authors have no Conflict of interest to declare that are relevant to the content of this article.

Open Access This article is licensed under a Creative Commons Attribution 4.0 International License, which permits use, sharing, adaptation, distribution and reproduction in any medium or format, as long as you give appropriate credit to the original author(s) and the source, provide a link to the Creative Commons licence, and indicate if changes were made. The images or other third party material in this article are included in the article's Creative Commons licence, unless indicated otherwise in a credit line to the material. If material is not included in the article's Creative Commons licence and your intended use is not permitted by statutory regulation or exceeds the permitted use, you will need to obtain permission directly from the copyright holder. To view a copy of this licence, visit http://creativecommons.org/licenses/by/4.0/.

References

1. Andrade JE (2009) A predictive framework for liquefaction instability. Géotechnique 59(8):673–682. https://doi.org/10.1680/geot.7.00087
2. Andrade JE, Ramos AM, Lizcano A (2013) Criterion for flow liquefaction instability. Acta Geotech 8(5):525–535. https://doi.org/10.1007/s11440-013-0223-x
3. Andrianopoulos KI, Papadimitriou AG, Bouckovalas GD (2010) Bounding surface plasticity model for the seismic liquefaction analysis of geostructures. Soil Dyn Earthq Eng 30(10):895–911. https://doi.org/10.1016/j.soildyn.2010.04.001
4. Azeiteiro RJ, Coelho PA, Taborda DM et al (2017) Critical state-based interpretation of the monotonic behaviour of Hostun sand. Am Soc Civ Eng. https://doi.org/10.1061/(ASCE)GT.1943-5606.0001659
5. Bandini V, Coop MR (2011) The influence of particle breakage on the location of the critical state line of sands. Soils Found 51(4):591–600. https://doi.org/10.3208/sandf.51.591
6. Been K, Jefferies MG (1985) A state parameter for sands. Géotechnique 35(2):99–112. https://doi.org/10.1680/geot.1985.35.2.99
7. Been K, Jefferies MG, Hachey J (1991) The critical state of sands. Geotechnique 41(3):365–381. https://doi.org/10.1680/geot.1991.41.3.365
8. Bolton MD (1986) The strength and dilatancy of sands. Geotechnique 36(1):65–78. https://doi.org/10.1680/geot.1986.36.1.65
9. Boulanger R, Ziotopoulou K (2015) Pm4sand (version 3): A sand plasticity model for earthquake engineering applications. Center for Geotechnical Modeling Report No UCD/CGM-15/01, Department of Civil and Environmental Engineering, University of California, Davis, Calif
10. Chu J, Leong W (2001) Pre-failure strain softening and pre-failure instability of sand: a comparative study. Géotechnique 51(4):311–321. https://doi.org/10.1680/geot.2001.51.4.311
11. Chu J, Wanatowski D, Leong W et al (2015) Instability of dilative sand. Geotech Res 2(1):35–48. https://doi.org/10.1680/gr.14.00015
12. Dafalias YF, Manzari MT (2004) Simple plasticity sand model accounting for fabric change effects. J Eng Mech 130(6):622–634. https://doi.org/10.1061/(ASCE)0733-9399(2004)130:6(622)
13. Dilip A, Adamidis O (2024) State parameter for partially drained paths using a sanisand model. Comput Geotech 170:106295. https://doi.org/10.1016/j.compgeo.2024.106295
14. Eliadorani A, Vaid Y (2005) Liquefaction of dilating sand. In: Earthquake engineering and soil dynamics, pp 1–11, https://doi.org/10.1061/40779(158)29
15. Eliadorani AA (2000) The response of sands under partially drained states with emphasis on liquefaction. PhD thesis, University of British Columbia
16. Fleminger R (2026) Experimental investigation of drainage effects around monopiles in sand. PhD thesis, University of Oxford
17. Hill R (1958) A general theory of uniqueness and stability in elastic-plastic solids. J Mech Phys Solids 6(3):236–249. https://doi.org/10.1016/0022-5096(58)90029-2
18. Imposimato S, Nova R (1998) An investigation on the uniqueness of the incremental response of elastoplastic models for virgin sand. Mech Cohesive-Frict Mater Int J Exp Modell Comput Mater Struct 3(1):65–87. https://doi.org/10.1002/(SICI)1099-1484(199801)3:1<65::AID-CFM42>3.0.CO;2-9
19. Jefferies MG (1993) Nor-sand: a simle critical state model for sand. Géotechnique 43(1):91–103. https://doi.org/10.1680/geot.1993.43.1.91
20. Jrad M, Sukumaran B, Daouadji A (2012) Experimental analyses of the behaviour of saturated granular materials during axisymmetric proportional strain paths. Eur J Environ Civ Eng 16(1):111–120. https://doi.org/10.1080/19648189.2012.666900
21. Kamai R, Boulanger R (2012) Single-element simulations of partial-drainage effects under monotonic and cyclic loading. Soil Dyn Earthq Eng 35:29–40. https://doi.org/10.1016/j.soildyn.2011.10.002
22. Kassas K, Adamidis O, Gerolymos N et al (2021) Numerical modelling of a structure with shallow strip foundation during earthquake-induced liquefaction. Géotechnique 71(12):1099–1113. https://doi.org/10.1680/jgeot.19.P.277
23. Lashkari A (2009) On the modeling of the state dependency of granular soils. Comput Geotech 36(7):1237–1245. https://doi.org/10.1016/j.compgeo.2009.06.003
24. Lashkari A, Yaghtin M (2018) Sand flow liquefaction instability under shear-volume coupled strain paths. Géotechnique 68(11):1002–1024. https://doi.org/10.1680/jgeot.17.P.164
25. Lashkari A, Falsafizadeh S, Rahman MM (2021) Influence of linear coupling between volumetric and shear strains on instability and post-peak softening of sand in direct simple shear tests. Acta Geotech 16(11):3467–3488. https://doi.org/10.1007/s11440-021-01288-5
26. Li XS, Dafalias YF (2000) Dilatancy for cohesionless soils. Géotechnique 50(4):449–460. https://doi.org/10.1680/geot.2000.50.4.449
27. Li XS, Dafalias YF (2012) Anisotropic critical state theory: role of fabric. J Eng Mech 138(3):263–275. https://doi.org/10.1061/(ASCE)EM.1943-7889.0000324
28. Li XS, Dafalias YF, Wang ZL (1999) State-dependant dilatancy in critical-state constitutive modelling of sand. Can Geotech J 36(4):599–611. https://doi.org/10.1139/t99-029
29. Liu H, Kementzetzidis E, Abell JA et al (2022) From cyclic sand ratcheting to tilt accumulation of offshore monopiles: 3d Fe modelling using Sanisand-MS. Géotechnique 72(9):753–768. https://doi.org/10.1680/jgeot.20.P.029
30. Logeswaran P (2005) Behaviour of sands under simultaneous changes in volume and pore pressure. PhD thesis, Carleton University
31. Nicot F, Daouadji A, Hadda N et al (2013) Granular media failure along triaxial proportional strain paths. Eur J Environ Civ Eng 17(9):777–790. https://doi.org/10.1080/19648189.2013.819301
32. Papadimitriou AG, Bouckovalas GD, Dafalias YF (2001) Plasticity model for sand under small and large cyclic strains. J Geotech Geoenviron Eng 127(11):973–983. https://doi.org/10.1061/(ASCE)1090-0241(2001)127:11(973)
33. Papadimitriou AG, Limnaiou TG, Chaloulos YK (2023) Benefits and pitfalls of advanced numerical modelling in earthquake geotechnical engineering. In: 10th European conference on numerical methods in geotechnical engineering, London, UK, 440, https://doi.org/10.53243/NUMGE2023-440
34. Poulos SJ (1981) The steady state of deformation. J Geotech Eng Div 107(5):553–562. https://doi.org/10.1061/AJGEB6.0001129
35. Roscoe KH (1963) A fundamental principle of similarity in model tests for earth pressure problems. In: Proceedings of the 2nd Asian regional conference on SMFE, pp 134–140
36. Roscoe KH, Schofield AN, Wroth CP (1958) On the yielding of soils. Geotechnique 8(1):22–53. https://doi.org/10.1680/geot.1958.8.1.22
37. Salimi M, Lashkari A, Tafili M (2024) Dem investigation on flow instability of particulate assemblies under coupling between volumetric and axial strains. Acta Geotech 19(11):7261–7286. https://doi.org/10.1007/s11440-024-02331-x

38. Schofield AN, Wroth P (1968) Critical state soil mechanic, vol 310. McGraw-hill, London
39. Sento N, Kazama M, Uzuoka R et al (2004) Possibility of postliquefaction flow failure due to seepage. J Geotech Geoenviron Eng 130(7):707–716. https://doi.org/10.1061/(ASCE)1090-0241(2004)130:7(707)
40. Sivathayalan S, Logeswaran P (2008) Experimental assessment of the response of sands under shear-volume coupled deformation. Can Geotech J 45(9):1310–1323. https://doi.org/10.1139/T08-068
41. Taiebat M, Dafalias YF (2008) Sanisand: Simple anisotropic sand plasticity model. Int J Numer Anal Meth Geomech 32(8):915–948. https://doi.org/10.1002/nag.651
42. Taiebat M, Jeremić B, Dafalias YF et al (2010) Propagation of seismic waves through liquefied soils. Soil Dyn Earthq Eng 30(4):236–257. https://doi.org/10.1016/j.soildyn.2009.11.003
43. Theocharis AI, Vairaktaris E, Dafalias YF et al (2019) Necessary and sufficient conditions for reaching and maintaining critical state. Int J Numer Anal Meth Geomech 43(12):2041–2055. https://doi.org/10.1002/nag.2943
44. Vaid YP, Eliadorani A (1998) Instability and liquefaction of granular soils under undrained and partially drained states. Can Geotech J 35(6):1053–1062. https://doi.org/10.1139/t98-061
45. Vaid YP, Eliadorani A (2000) Undrained and drained (?) stress-strain response. Can Geotech J 37(5):1126–1130. https://doi.org/10.1139/t00-036
46. Verdugo R, Ishihara K (1996) The steady state of sandy soils. Soils Found 36(2):81–91. https://doi.org/10.3208/sandf.36.2_81
47. Wan R, Guo P (1998) A simple constitutive model for granular soils: modified stress-dilatancy approach. Comput Geotech 22(2):109–133. https://doi.org/10.1016/S0266-352X(98)00004-4
48. Wanatowski D, Chu J (2011) Pre-failure instability behavior of sand in strain path testing under plane-strain conditions. Soils Found 51(3):423–435. https://doi.org/10.3208/sandf.51.423
49. Wang ZL, Dafalias YF, Li XS et al (2002) State pressure index for modeling sand behavior. J Geotech Geoenviron Eng 128(6):511–519. https://doi.org/10.1061/(ASCE)1090-0241(2002)128:6(511)
50. Wu Q, Xu T, Yang Z (2020) Diffuse instability of granular material under various drainage conditions: discrete element simulation and constitutive modeling. Acta Geotech 15(7):1763–1778. https://doi.org/10.1007/s11440-019-00885-9
51. Yang M, Taiebat M, Dafalias YF (2022) Sanisand-MSF: a sand plasticity model with memory surface and semifluidised state. Géotechnique 72(3):227–246. https://doi.org/10.1680/jgeot.19.P.363

Publisher's Note Springer Nature remains neutral with regard to jurisdictional claims in published maps and institutional affiliations.